Thermodynamics and transport of protons in functional oxides

Thesis submitted for the degree of *Philosophiae Doctor*

By

Christian Kjølseth

FERMiO – Functional Energy Related Materials in Oslo

SMN – Centre for Materials Science and Nanotechnology

Department of Chemistry

Faculty of Mathematics and Natural Sciences

University of Oslo

Preface

This thesis is part of the work for the degree of Philosophiae Doctor (PhD) at the Centre for Materials Science and Nanotechnology, Department of Chemistry, University of Oslo (UiO), Norway. The work has been carried out during the period of August 2005 to July 2009 under the supervision of Associate Professor Reidar Haugsrud and Professor Truls Norby, both UiO.

I would like to express my gratitude to my supervisors Professor Truls Norby and Associate Professor Reidar Haugsrud. Professor Truls Norby has been my main supervisor and his continuous optimism, encouragement and scientific guidance has been extremely valuable to me. Associate Professor Reidar Haugsrud has been particularly helpful and has always been ready to discuss scientific problems and results, as well as giving inspiration through the thesis. I am also thankful for the help and support from fellow students and colleagues at the group for Solid State Electrochemistry at Functional Energy Related Materials in Oslo, and want to call special attention to Harald Fjeld, who has always listened to and discussed my scientific topics and thoughts as well as being a good friend, and to Skjalg Erdal, who has been easy to collaborate with on a difficult subject. I would also like to especially thank the following persons who have contributed to make this thesis possible: Lin-Yung Wang, Tor Svendsen Bjørheim and Paul Inge Dahl.

I am very grateful to my family. My parents, sister and brother have contributed me with their confidence. Victoria, my daughter, has inspired me to find new values in life. And, finally, I want to thank Rebecca, you have been patient, supporting and very important to me during this rather demanding period.

July 2009
Christian Kjølseth

CONTENTS

Contributions to other publications and manuscripts during the PhD project but not included in this thesis:

- M.L. Fontaine, Y. Larring, M. Fleissner, C. Estournès, C. Kjølseth, T. Ø. S. Andersen, K. Wiik, R. Bredesen, **"Developments in Proton Conducting Membranes for Hydrogen Separation and Fuel Cell Applications"**, Proceedings AIChE Annual Meeting 2006

- R. Haugsrud, C. Kjølseth, "**Effects of protons and acceptor substitution on the electrical conductivity of La_6WO_{12}"**, Journal of Physics and Chemistry of Solids, 69 (2008) 1758

- T. Norby, C. Kjølseth, R. Strandbakke, M.L. Fontaine, **"Protonics for Fuel Cells",** Proceedings Luzerne Fuel Cell Forum (2009)

- L-Y. Wang, C. Kjølseth, N. Jalarvo, R. Haugsrud, T. Norby, **"Stability study of ternary oxides investigated by TG-DSC"** in preparation

SUMMARY

The present project addresses several interrelated issues in understanding hydrogen's role in functional oxide materials – both in grain interior and grain boundary – with focus on its role as dopant, its solubility, and its transport properties.

The grain boundaries in many of the most studied ceramic proton conductors have an intrinsic resistance much higher than the grain interior resistance. This has been proposed to originate from a charged grain boundary core with adjacent space charge layers. The specific electrical conductivity of the grain boundaries in 10 % Y-doped $BaZrO_3$ (BZY10) and nominally undoped $BaZrO_3$ obtained from impedance spectroscopy and the brick layer model, showed a high proton resistivity. The conductivity in the grain interior and grain boundaries were measured as a function of oxygen partial pressure and under reducing conductions it showed an additional n-type electronic conductivity in the grain boundaries. This observation indicated that electrons accumulated in the space charge layers as partial compensation of the positively charged grain boundary core. This was supported by a careful TEM analysis on the doped samples where also an accumulation of the negatively charged Y-dopants in the grain boundaries was observed.

A space charge model, frequently used for oxide ion conductors, was applied to analyse the behaviour of the grain boundaries of BZY10. Calculations of the space charge layer defect profile gave insight in the magnitude of the depletion of protons. The profile showed an increasing proton resistance towards the grain boundary core, which was suggested to cause a distortion in the grain boundary arc in the impedance spectrum. Schottky barrier heights, which is the measure of the space charge effect, were calculated under different conditions. For a spark plasma sintered BZY10 sample, it was found to be 0.51 V and for a hot pressed sintered BZY10 sample 0.62 V at 300 °C in a humidified oxygen atmosphere. Under dry conditions the spark plasma sintered sample showed a Schottky barrier height higher under dry conditions compared to wet, which was suggested to stem from a hydration of grain boundary core oxygen sites at the cost of grain interior oxygen vacancies. An additional feature observed for the undoped case was a larger ratio of p-type electronic to protonic conduction in the grain boundaries as compared to the doped cases, contrary to the prediction of simple defect chemistry and space charge theory.

In systems where effectively negative cations, i.e. acceptors, have been substituted to increase the concentration of native charge compensating positive defects (oxygen vacancies, $v_O^{\bullet\bullet}$) protons can dissolve as hydroxide defects ($OH_O^{\bullet}$), when the positive defects interact with water vapour in the surrounding atmosphere. The standard molar hydration enthalpy of this reaction, the hydration of oxygen vacancies in oxides, has been studied for the first time with a combined thermogravimetric-calorimetric approach using a novel TG-DSC instrument which can operate at high water vapour pressures. The chosen materials were two of the most studied proton conducting perovskite oxides, BZY10 and 10 % Y-doped $BaCeO_3$ (BCY10). The measurements were done isothermally for parallel recording of the weight change and the heat-exchange associated with step changes in the water vapour pressure surrounding the specimen. The obtained molar hydration enthalpy of BZY10 was investigated at 300-900 °C

and was found constant at -81±4 kJ mol^{-1} (per mole of H_2O) over this range. The molar hydration enthalpy of BCY10 was investigated at 600 °C and found to be -170±6 kJ mol^{-1}. Both values are in good agreement with the majority of literature data obtained by indirect equilibrium methods on the two materials. This gives confidence in the applicability of both experimental approaches, and suggests that TG-DSC may be used for further refinement of the correlations and understanding of the thermodynamics of hydration of oxides.

It is widely accepted that hydrogen acts as a shallow donor in ZnO and that hydrogen thereby is the source of the observed prevailing n-type conductivity in undoped ZnO. However, most work on the electrical properties of ZnO is conducted at low temperature. The electrical properties have in this work therefore been investigated at higher temperatures, where the hydrogen in ZnO is initially in equilibrium with the surrounding gas mixture. This has been done via electrical conductivity and thermoelectric measurements in H_2+H_2O+inert gas atmospheres at temperatures up to 500 and 550 °C, respectively. The concentration of electrons and their charge compensating protonic defect were determined from the thermoelectric power, and electron charge mobility was evaluated by combination with the measured conductivity. Above ~450 °C, the defects were in equilibrium with the surroundings, and the concentration of protons and electrons increased with temperature and with $p_{H_2}^{1/4}$, in accordance with the defect thermodynamics from literature. Hydrogen was found to freeze in at temperatures below ~450 °C, which resulted in a high internal hydrogen pressure during further cooling. The local strain from the presence of frozen in neutral H_2 species was suggested to cause an observed modest reduction in the mobility and conductivity of electrons. The levels of defect concentrations and electron mobility were one order of magnitude too high and low, respectively, compared with established literature when based on our thermoelectric power, applying standard theory of a free electron gas.

1. INTRODUCTION

Functional materials are central in tomorrow's technologies based on renewable energy. Important technologies needed to take hydrogen into use and to achieve a more efficient use of fossil fuels comprise fuel cells and electrolysers, gas separation membranes, catalytic reactors, and hydrogen storage. This work and thesis deal with functional materials used in components for these technologies, with focus on the role of hydrogen, and with oxides as the main hosts. In general, the choice of oxidic hosts enables use at high temperatures and thus favours kinetics and thermal integration.

One such class of materials, where knowledge of the behaviour of hydrogen is decisive, is proton conducting oxides. Traditionally, solid electrolytes are based on oxide ion conducting oxides or proton conducting polymers. These materials face challenges when it comes to a high operating temperature (typically > 800 °C) for the oxide ion conductors and low temperature (< 100 °C) for the polymers where liquid water is part of the transport process. Proton conducting oxides have highest conductivity in an intermediate range, 400 – 800 °C, which is favourable when it comes to the combination of good kinetics and a wide selection of durable materials for electrodes and especially interconnects.

A particular problem with many proton conducting oxides is a high grain boundary resistance [1]. It is often uncertain whether this is due to low mobility or low concentration of protons in the grain boundaries. It is, however, probable that the charged core of the grain boundary and the space charge region around it may affect the concentration of protons. The investigation of this is a central part of the thesis.

Proton conducting oxides take up protons from ambient water vapour to charge compensate acceptor dopants. Based on deconvolution of proton concentration or proton conductivity vs. temperature, a large number of sets of entropies and enthalpies for this hydration reaction have been extracted in the literature. From these data, correlations of the hydration enthalpy have been suggested [1, 2], however, the uncertainties involved in the experimental approaches give rise to large scatter in the correlations. The hydration thermodynamics thus need to be measured directly by calorimetric methods. In this thesis such a method is investigated and used to measure the standard molar hydration enthalpy of selected state-of-the-art proton conductors.

Hydrogen also plays a role in many semiconductors that are currently receiving much scientific attention such as SiC and ZnO, essential for novel electronic components, solar cells and sensors. Here, hydrogen may act as defect terminators or dopants, playing a decisive role on the electrical properties. Hydrogen is omnipresent in fabrication processes, and is as such an element whose impact on the electrical and optical properties of materials is of great importance to understand. Reports on hydrogen in ZnO have shown that hydrogen behaves differently here compared to in traditional semiconductors [3]. Most work on the electrical properties of ZnO is conducted at low temperatures; our aim is to examine the electrical properties at temperatures where the hydrogen in our sample is initially in equilibrium with the surrounding atmosphere.

The thesis is based on work in three different related fields regarding the abovementioned subjects. The first part will deal with transport of protons in polycrystalline materials with focus on the grain boundaries. The second part will deal with fundamental thermodynamics of the hydration of proton conductors, while the last part will deal with both thermodynamics and transport of protons in ZnO. Each part will in the following be introduced, in order to present the relevance, methodology, and goals of each.

1.1 Protons in grain boundaries

Grain boundaries in ionically conducting oxides normally have a higher electrical resistance than the grain interior (in many other ionic conductors the grain boundaries act as highly conducting channels). The grain boundary resistance generally increases more than the grain interior resistance with decreasing temperature. In the operating temperature of the proton conducting fuel cells the grain boundary resistance dominates the total DC electrolyte resistance, and lowers the performance of the fuel cell. It is therefore desired to understand and if possible decrease the grain boundary resistance of proton conducting oxides.

Attributing the grain boundary resistance in ionic conductors to intergranular siliceous phases was dominating in the literature (see e.g. [4-6]) until it was gradually realized that space charge effects, probably due to an accumulation of oxygen vacancies in the grain boundary core, contributed to the resistance (see e.g. [7-9]). A challenge has been to experimentally and directly identify the space charge effect, however it seems that currently there is a general acceptance that such an effect is operative. Almost all work has, so far, been conducted on oxide ion conductors and mixed oxide ion – electron conductors (see e.g. [10-15]), and very little in this direction has been done on proton conductors. A goal of the present thesis is therefore to apply space charge theory to proton conductors, and to search for experimental indications of a space charge effect.

An impedance spectrum of the state-of-the-art proton conductor Y-doped $BaZrO_3$ is given in Fig. 1.1. The arc in the inserted figure is a result of the impedance of the grain interior while the arc in the large figure is a result of the impedance in the grain boundaries. The relative magnitude of the arcs reflects the resistance. It is evident that the grain boundary resistance in Y-doped $BaZrO_3$ is very large compared to the grain interior resistance, and considering how thin the grain boundaries are, the relative specific resistivity must be even larger. Y-doped $BaZrO_3$ was therefore chosen as the proton conductor of which the grain boundaries are to be studied.
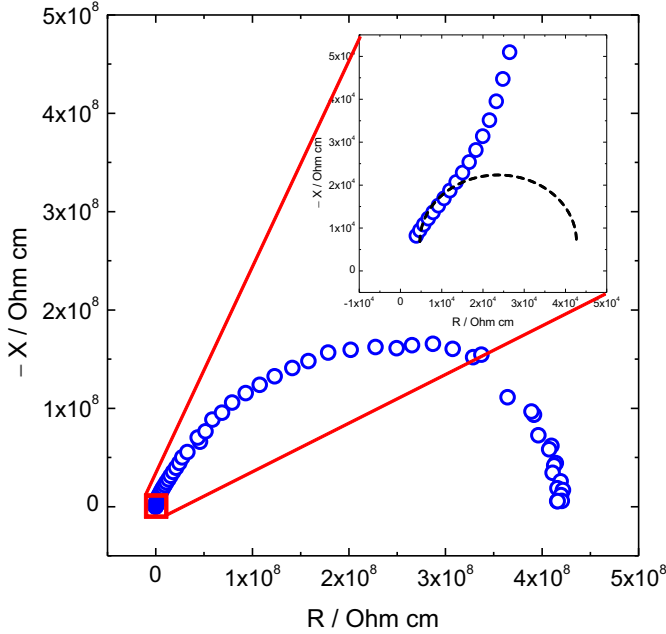
Fig. 1.1. Impedance spectrum of $BaZr_{0.9}Y_{0.1}O_{3-\delta}$ in wet O_2 at 225 °C. The magnified part shows the grain interior contribution, where the dotted line indicates the grain interior impedance arc.

1.2 Hydration of acceptor-doped oxides – calorimetric studies

As the protonic defect is effectively positive, its concentration is enhanced by acceptor-doping. Work on proton conductors has therefore almost exclusively been done on acceptor-doped oxides. In these oxides the acceptors are generally compensated by oxygen vacancies in the dry state (which consequently increases the oxide ion conductivity), however, when equilibrated in water vapour the oxides dissolve protons and fill the vacancies, according to the following defect chemical reaction

$$H_2O(g) + v_O^{\bullet\bullet} + O_O^x = 2OH_O^{\bullet} \qquad (1)$$

The standard molar hydration entropy and enthalpy, determine the solubility of water under given conditions. Generally, the enthalpy is negative, which implies that protons dominate at low temperatures and oxygen vacancies at high temperatures. Hydration enthalpies have usually been derived from thermogravimetry (TG) and conductivity measurements. The values vary considerably, with some apparent correlation to materials properties. In rare earth sesquioxides the enthalpy becomes more negative as the oxide gets more stable (the enthalpy of formation gets more negative), which was attributed to higher stability of competing oxygen vacancies in the more unstable oxides [16]. For perovskites several attempts have

5

been made to correlate the standard molar hydration enthalpy to materials properties [1, 2, 17]. However, common to all suggested correlations is that they at present contain much scatter. This is most probably partly due to the questionable quality of data from deconvoluting and fitting equilibrium measurements (e.g. TG and conductivity) to entropies and enthalpies over limited temperature ranges.

Efforts to measure the molar hydration enthalpy by calorimetric techniques have been performed in our group with mixed results [18]. Although calorimetric signals of the hydration reaction have been obtained, it has been difficult to estimate the corresponding water uptake (i.e. the hydration enthalpy has been obtained, but not the molar hydration enthalpy). The ideal technique to measure the standard hydration enthalpy would therefore be a combined themogravimetric and calorimetric technique utilizing for instance a TG-DSC (thermogravimetry – differential scanning calorimetry) instrument where molar enthalpies can be obtained directly. The goal of the present work is to test whether the standard molar enthalpy can be obtained using such an instrument, and if successful, measure the standard molar hydration enthalpy of the state-of-the-art proton conductors Y-doped $BaZrO_3$ and Y-doped $BaCeO_3$.

1.3 Protons in ZnO

ZnO is of interest for a range of electro-optical applications. In this oxide, hydrogen dissolves and acts as a dominating electron donor as it is ionized to protons. This is illustrated in Fig. 1.2 where the electronic conductivity of single crystal ZnO is plotted as a function of temperature and hydrogen pressure given by Thomas and Lander [19], is presented. The electronic conductivity increases with increasing hydrogen pressure, indicating the direct relation between n-type conductivity and hydrogen solubility.
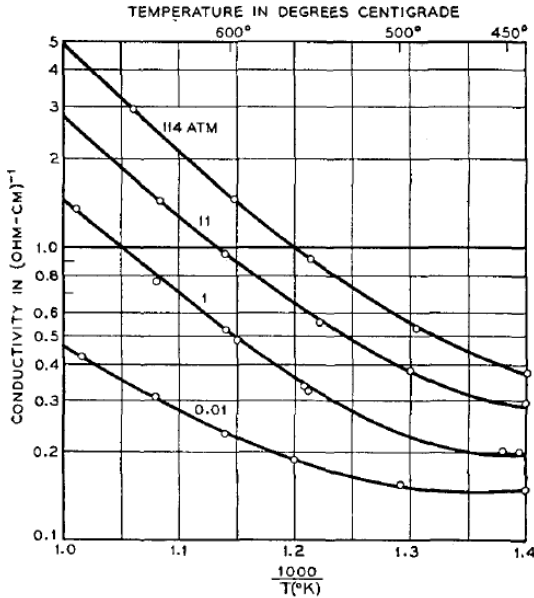
Fig. 1.2. Electronic conductivity of a ZnO single crystal as a function of temperature and hydrogen pressure. From Thomas and Lander [19].

While the proton conductivity in ZnO is too low to be utilized, the donated electrons, which dominate the electrical properties makes the material a reasonably good n-type conductor. It is in fact difficult to effectively acceptor-dope the material to a p-type conductor, needed in semiconductor applications, because of the omnipresent hydrogen from hydrogen gas or water vapour. Therefore, a full understanding of the presence, behaviour, and role of hydrogen is essential under all conditions.

Generally, the hydrogen is dissolved under equilibrium with a $H_2(g) + H_2O(g)$ atmosphere at high temperature. One goal is to obtain the parameters for the defect equilibria that govern the concentrations of protons and other hydrogen species. The concentration of protons is obtained from the concentration of the charge compensating electrons, which, in turn, we will attempt to obtain from the thermoelectric power. For this it is necessary to understand the entropy of electrons in ZnO. Eventually, the concentration of electrons can be combined with measured conductivity, and the electron mobility can be obtained. While both the mobility and concentration of electrons and protons were reported already by Hutson [20] and Thomas and Lander [19] in the 1950s, our goal is to verify and hopefully refine the model of dissolution and transport of protons and electrons in ZnO under reducing, H_2-containing conditions, and to extend the application of the parameters obtained in order to predict equilibrium concentrations of protonic and electronic defects also at higher oxygen activities.

1.4 The structure of the thesis

The thesis is built up of introductory parts on the individual subjects, followed by a number of manuscripts under publication or in the process of being submitted. The last part of the thesis includes discussions on individual parts as well as an overall discussion and a conclusion. The introductory and last part contains experimental details, discussions, and speculations that have been too extensive for the format of the scientific manuscripts. However, to avoid repetition, these parts to a large extent exclude theory, normal experimental information, results, and discussion which are described in the manuscripts. The introductory part, manuscripts, and final discussions thus complement each other and should be read equally. Only on H in ZnO will the thesis not have an additional part, as the manuscript already contains relatively exhaustive introduction and discussion. Still, the role of hydrogen in ZnO will be taken into account in the final general discussion.

2.   GRAIN BOUNDARY RESISTANCE IN PROTON CONDUCTORS

From an application point of view it is more important to decrease the grain boundary resistance in proton conductors compared to that in oxide ion conductors. The difference in grain boundary and grain interior activation energy makes the grain boundary resistance more pronounced at the lower operating temperature of the proton conducting fuel cell. In addition, as seen in MANUSCRIPT I, the relative specific grain boundary resistance seems also to be higher for the state-of-the-art proton conductors compared to the oxide ion conductors. Any extrinsic source of the grain boundary resistance is ruled out, such as silica impurity phases, and only the intrinsic origin of the grain boundary resistance, where a grain boundary core-space charge model is central, is treated (which is reasonable since no impurities were detected with SEM or high resolution TEM, see MANUSCRIPT I and II).

It is probable that the charge of the core of the grain boundary and the space charge region around may affect the concentration of protons (this is in line with the current interest in interfaces which is important in the field of nanoionics [7, 21]). A grain boundary core-space charge layer model has been applied on several oxide ion conductors, such as acceptor-doped ZrO_2 [22] , CeO_2 [13, 23], $LaGaO_3$ [14] and $SrTiO_3$ [9, 24]. For proton conductors little experimental work has been reported. The present thesis seeks to investigate experimentally whether space charge layers exist in the proton conductor acceptor-doped $BaZrO_3$. MANUSCRIPT I gives a theoretical overview of space charge theory for proton conducting oxides, so the general theory will not be included here. MANUSCRIPT II also discusses the grain boundary properties of acceptor-doped $BaZrO_3$ together with nominally undoped $BaZrO_3$.

The general understanding and the experimental approaches of the space charge effect in oxides have been treated in a number of publications of the mentioned oxide ion and mixed conductors above. Some of the experimental approaches used in these publications will be treated in the following. However, first the thermodynamics of the grain boundaries needs to be discussed to understand the origin of space charge layers. Then some space charge concentration profiles for charged species in a proton conductor are sketched to provide a simple picture of the effect. The literature on space charge effect in proton conductors is rather scarce, although some papers include results which can be used to derive information on the space charge effect. In the present thesis some of these results have therefore been extracted and used to calculate the space charge potentials. This grain boundary section ends up with a part where the peculiar distortion in the grain boundary arc of an impedance spectrum is simulated by a finite element approach in light of the space charge effect.

2.1 Grain boundary thermodynamics

A grain boundary serves as a sink for point defects. The concentration of each point defect, both in the grain boundary core and in its vicinity, is controlled by its individual Gibbs energy of formation in the various locations. In general, adding up all defect charges in the grain boundary core results in a non-vanishing space charge density in the grain interior with

an equal charge of opposite sign as the grain boundary core. This charge dipole generates a potential difference between the grain interior and the grain boundary core so that an electrostatic energy contribution is added to the Gibbs energy of defect formation. The electrostatic energy contribution counteracts the initial differences between the individual defect formations energies until all defect concentrations are balanced, such that local charge neutrality is achieved inside the grain interior at sufficient distance from the grain boundary core [8]. As a result, the concentrations of charged point defects are not constant over the cross-section of a grain but deviate from their grain interior values in the vicinity of grain boundaries. In almost all practical cases, it is likely that the equilibrium is influenced by the effective charge of the aliovalent dopants and/or impurities that accumulate in the space charge layers [11].

2.2 Grain boundary core-space charge layer model

The grain boundary core-space charge layer model is as mentioned above derived for proton conductors in MANUSCRIPT I and in general by Kim et al. [13], and will therefore not be treated in detail here. However, in Fig. 2.1 a schematic representation is given of a grain boundary consisting of a positive grain boundary core which is charge compensated by two adjacent space charge layers. It also indicates the potential profile and the value of the Schottky barrier height, $\Delta\varphi(0)$. This potential is the potential at the core space charge layer intercept relative to grain interior ($\Delta\varphi(0) = \varphi(0) - \varphi(\infty)$). For ionic conductors mentioned in this thesis an increasing potential yields an increasing specific grain boundary resistance. Fig. 2.2 shows sketches of different concentration profiles which are applicable to proton conductors dealt with in the present thesis.
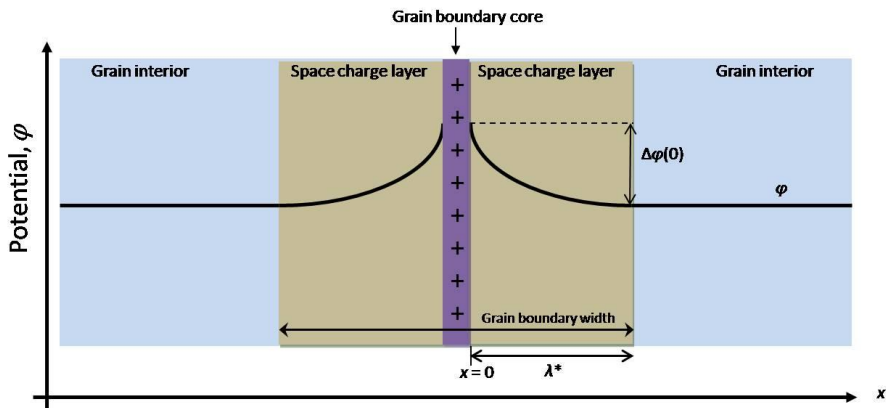
Fig. 2.1. Schematic representation of a grain boundary consisting of a positive grain boundary core charge compensated by two adjacent space charge layers. Values of x are defined such that far into the grain interior $x = \infty$ while at the interface between the space charge layer and the grain boundary core $x = 0$. The line represents the potential profile and the Schottky barrier height potential difference, $\Delta\varphi(0)$, is indicated.
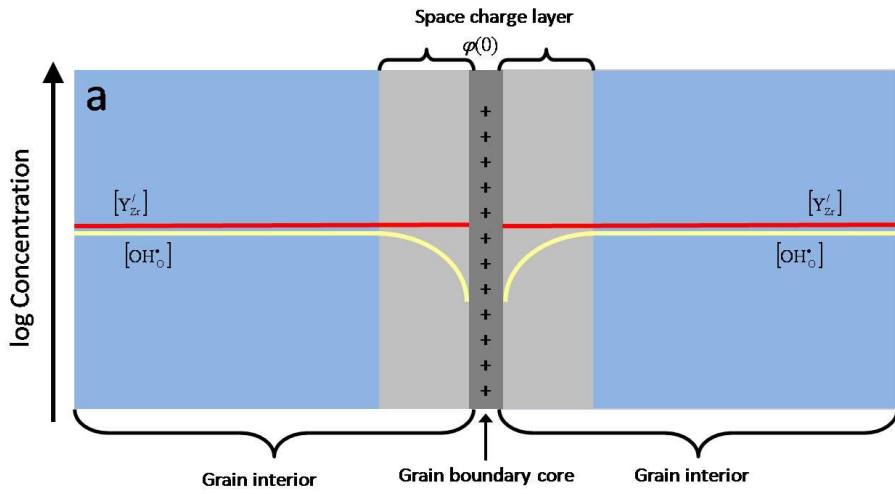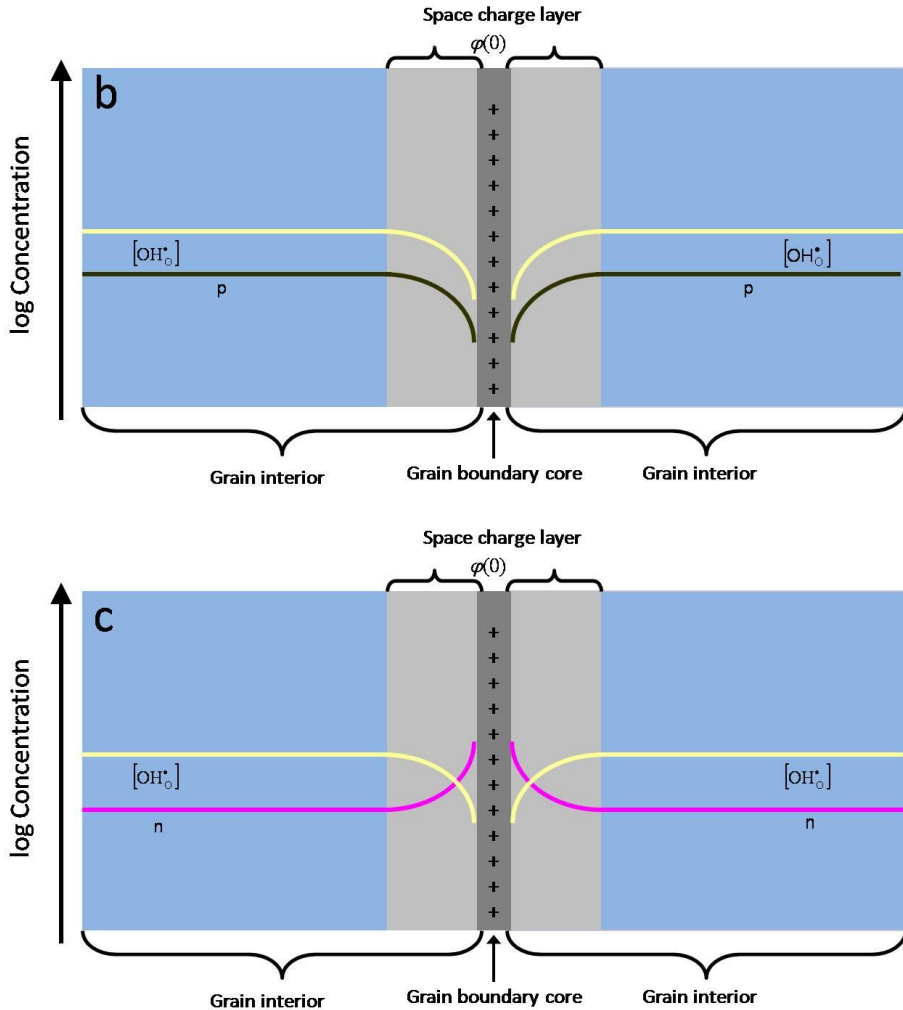
Fig. 2.2. Sketches of possible concentration profiles in the space charge layer (dopant level not shown in b and c). a: Depletion of protons in the space charge layer while the acceptor concentration is assumed to be constant through the sample (Mott-Schottky approximation). b: Both protons and electron holes follow the same concentration profile in the space charge layer because of the same charge. c: Electrons accumulates while protons deplete in the space charge layer which leads to a change in conductivity from protonic in grain interior to electronic in the grain boundary.

In Fig. 2.2a, the defect profile of the acceptor dopant $Y_{Zr}^{/}$ is assumed to be constant up to the grain boundary core (Mott-Schottky approximation), and the protons are depleted in the space charge layers. This situation is dominating for proton conductors where the proton transport number is unity. In Fig. 2.2b we see that the protons and electron holes follow the same concentration profile. Consequently, the electron holes will in principle never become the prevailing conductive species in the grain boundaries of a proton conductor. In the last sketch, Fig. 2.2c, the opposite charge of the electrons to the protons can yield a proton conducting

grain interior and an electron conducting grain boundary. The electrical conductivity changes from being ionic in the grain interior to becoming electronic in the grain boundary. Because of the positive charge in the grain boundary core, as seen in all three cases, the protonic grain boundary resistance will be higher than compared to grain interior.

2.3 Space charge layer literature

Generally space charge effects are considered to affect all interfaces of ionic conductors, such as ionic conductor-insulator, ionic conductor(I)-ionic conductor(II), grain boundary interfaces and ionic conductor-gas interfaces [7]. Only the grain boundary interface is treated in the present work. When it comes to literature on the effect of space charge layers on the electrical properties of grain boundaries in ionic conductors, an appreciable amount of work has been done on oxide ion conductors. The main techniques used to identify and measure the space charge effect in grain boundaries of oxide ion conductors will be reviewed, followed by a short section where the space charge potential, the Schottky barrier height, of the same oxide ion conductors are discussed.

2.3.1 Experimental observations of the space charge effect

A review by Guo and Waser [11] on the electrical properties of the grain boundaries of acceptor-doped ZrO_2 and CeO_2 revises several experimental indications on the space charge effect. Of particular importance is an observation of non-linear grain boundary electrical properties as a function of dc bias voltage [25, 26], which is caused by the shortening of one space charge layer and the extension of the other in the bias direction. To identify a non-linear dependence, one needs to know the voltage drop over a single grain boundary. To be able to measure this voltage drop usually quite high applied voltages are needed (e.g. ~15 V), and a sample with few grain boundaries is advantageous (thin sample with large grains). We have in fact tested this for the proton conductor BZY10 [27], but despite indications of non-linearity, the voltage drop over a single grain boundary was considered to be lower than what is necessary to alter the space charge layers (grain size was too small compared to the sample thickness). Another experimental observation is electron accumulation in the space charge layers. In both acceptor-doped ZrO_2 [10] and CeO_2 [23, 28] this is experimentally observed as a p_{O_2}-dependence for the grain boundary conductivity under reducing conditions. It is also numerically simulated in $SrTiO_3$ [9] where the grain boundaries showed n-type conduction and the grain interior oxide ion conduction. Owing to the positive charge of the grain boundary core, electrons, as a result of their negative charge, accumulate in the space charge layers. This effect is prominent at low oxygen partial pressures, high temperatures and high space charge potentials. In Sr-doped $LaGaO_3$ a similar effect was found under oxidizing conditions; an increased electron-hole conduction was observed due to the fact that the oxygen vacancy depletes more steeply than electron holes [14]. The p_{O_2}-dependencies in this work was part of a quantitative analysis (based on the Mott-Schottky approximation) of the conductivity behaviour under various oxygen partial pressures and temperatures. A

quantitative analysis gives the partial conductivities of the grain boundary and grain interior conductivities which directly can say whether space charge layers contribute or not. Applying such an analysis on proton conductors would show a difference in grain interior and grain boundary transport number under reducing conditions, and in cases where oxide ions contribute under oxidizing conditions.

2.3.2 Space charge potential in oxide ion conductors

Table 1 displays a selection of Schottky barrier heights at 300 °C taken from literature. The somewhat deviating higher Schottky barrier height for Fe_2O_3-doped $SrTiO_3$ might be explained by the lower dopant concentration compared to the others. For Y_2O_3-doped CeO_2 an increase in the Schottky barrier height with decreasing dopant concentration [23] was observed. Qualitatively the acceptor dopant in the grain boundary core compensates more of the positive charge. Another feature worth mentioning observed for the oxide ion conductors is an increase in the Schottky barrier height with increasing temperature [22, 23]. Intuitively the Schottky barrier height should decrease with increasing temperature, since the space charge effect decreases with temperature. However taking the k_BT term in the calculation of the Schottky barrier height (Eq.(2) given in the next section) into account the observed behaviour is reasonable. The values in Table 1 are generally lower than the 0.50 V obtained for BZY10 in MANUSCRIPT I, which indicates that the grain boundary resistance in BZY10 is larger than that observed for the oxide ion conductors.

Table 1. Selection of Schottky barrier heights at 300 °C.

Material	Schottky barrier height	Reference
8 mol% Y_2O_3 doped ZrO_2	0.23 V	[22]
10 mol% Y_2O_3 doped CeO_2	0.30 V	[23]
1 mol% SrO doped $LaGaO_3$	0.4 V	[14]
0.4 mol% Fe_2O_3 doped $SrTiO_3$	0.63 V	[29]

2.4 Grain boundary literature of proton conductors

Generally the available literature on proton conducting oxides suffers from inconsistent grain boundary conductivities in that non-specific values are usually reported. This complicates the possibility to compare available data. To the authors' knowledge, only a few papers exist which report specific grain boundary electrical properties of proton conductors [30-32]. It is quite surprising that none of these papers are included in a recent review of the grain boundary electrical properties of proton conductors by Park et al. [33]. Fig. 2.3 shows how the grain boundary specific conductivities measured by Babilo et al. [30], Iguchi et al. [32] and Duval et al. [31] (only the sample sintered at 1720 °C) vary with inverse temperature. Specific grain boundary conductivity of the zone annealed sample (sintered at 2200 °C) reported by Duval et al. in the same paper is not included because the calculated

specific grain boundary conductivities was based on an assumption of a constant ratio between the grain interior and grain boundary capacitance. This assumption resulted in higher specific grain boundary conductivity at temperatures above ~500 °C, which, according to the brick layer model (BLM) can not be determined by impedance spectroscopy [34]. A similar assumption was made for the sample sintered at 1720 °C, which makes also these reported specific grain boundary conductivities questionable.
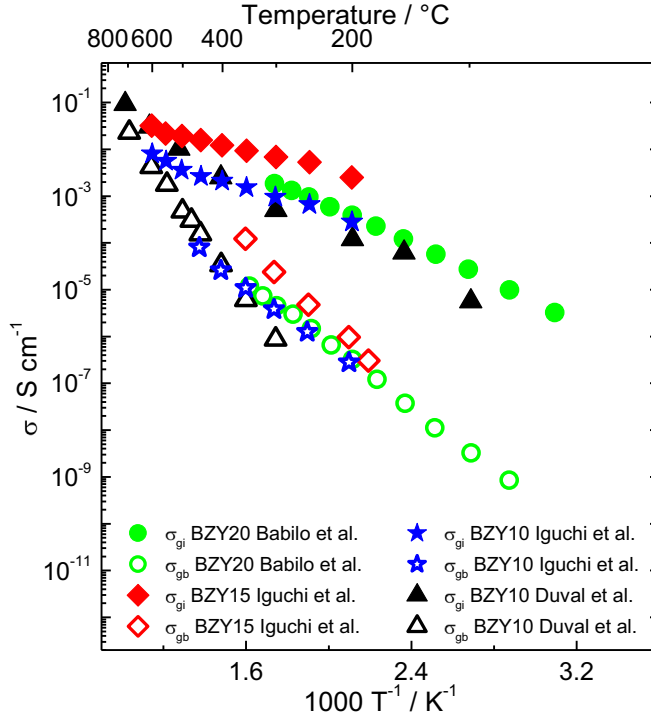
Fig. 2.3. Grain interior and specific grain boundary conductivities obtained experimentally on BZY20 by Babilo et al. [30] , on BZY10 and BZY15 by Iguchi et al. [32] and on BZY10 by Duval et al. [31].

As we see in Fig. 2.3 both the grain interior and specific grain boundary conductivities lie in the same range, but with relatively large differences, mainly due to the different doping levels, but also probably due to the difficulties in the processing of $BaZrO_3$ compounds as discussed by Babilo et al. [30]. From these curves we have calculated Schottky barrier heights through the following formula

$$\frac{\sigma_{gi}}{\sigma_{gb}} \cong \frac{\exp\left(\frac{e\Delta\varphi(0)}{k_B T}\right)}{\frac{2e\Delta\varphi(0)}{k_B T}} \qquad (2)$$

where σ_{gi} and σ_{gb} denote the grain interior and grain boundary conductivity, respectively, $\Delta\varphi(0)$ is the Schottky barrier height and e, k_B and T have their usual meaning. This formula is derived in MANUSCRIPT I. In Fig. 2.4 the Schottky barrier heights are plotted against dopant concentration, and in Fig. 2.5 as a function of temperature. As mentioned above, a decrease in the Schottky barrier with increasing dopant concentration and an increase in the Schottky barrier height with increasing temperature were observed for the oxide ion conductors. As seen in Fig. 2.4 and Fig. 2.5 none of these observations can clearly be observed for Y-doped BaZrO$_3$.
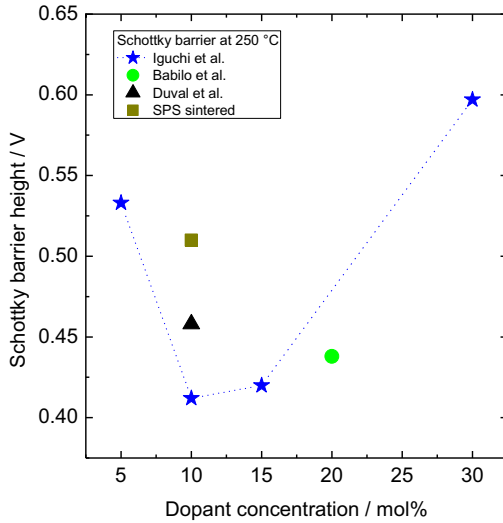

Fig. 2.4. Calculated Schottky barrier heights as a function of dopant concentration in Y-doped BazrO$_3$ based on conductivities from Iguchi et al. [32], Babilo et al. [30] and Duval et al. [31]. Values obtained from the SPS sintered sample given in MANUSCRIPT I is also included.
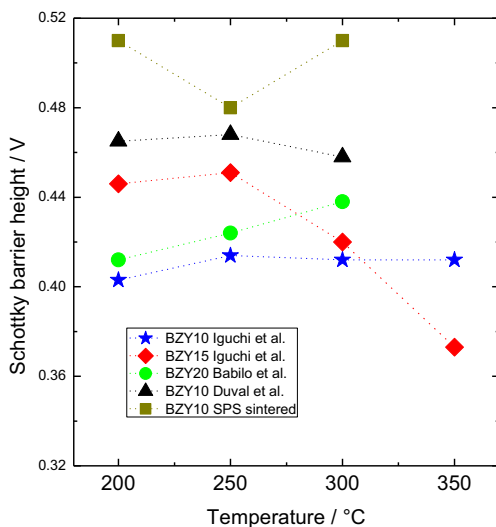
Fig. 2.5. Calculated Schottky barrier heights as a function of temperature based on conductivities for Y-doped BaZrO₃ from Iguchi et al. [32], Babilo et al. [30] and Duval et al. [31]. The Schottky barrier heights obtained from the SPS sintered sample is also included (see MANUSCRIPT I).

The scattering of the data indicates that either the experimental work on the proton conductors suffers from experimental inaccuracies or that the Schottky barrier height behaves differently in proton conductors compared to oxide ion conductors. Acceptor-doped BaZrO₃ has as mentioned proven to be difficult to process reproducibly with respect to proton conductivity as discussed in the work of Babilo et al. [30] where they strived to get reproducible results. In fact the conductivities in that work yielded the only Schottky barrier heights which follow the behaviour of the oxide ion conductors with increasing temperature, see Fig. 2.5. Experimental inaccuracies can therefore be a reason for the inconsistent behaviour, and possible dependencies may hide within the uncertainties of the measurements. In Fig. 2.4 we see that the Schottky barrier heights reported for BZY10 are in the range 0.4 – 0.5 V, which also indicates experimental inaccuracy. Still, a fundamental difference between oxide ion conductors and proton conductors must be considered. As we will see in section 5.1 there is presumably a difference when a possible hydration of the grain boundary core is taken into account.

2.5 Space charge and impedance spectroscopy

Impedance spectroscopy is an essential technique when it comes to studying the electrical properties of the grain boundaries. While the specific capacitance of the grain boundary may be similar to that in grain interior, the thickness is widely different and the grain boundary thus gives rise to an additional arc in the impedance spectrum, occurring at

lower frequencies. However, the technique is only applicable when the grain boundaries are more resistive than the grain interior. Furthermore, to get the specific grain boundary resistivities usually a brick layer model (BLM) needs to be applied. All these aspects are carefully described in [34]. Acceptor-doped $BaZrO_3$ shows a large grain boundary arc and a small grain interior arc which reflects its high grain boundary resistance (see Fig. 1.1). In addition to this we observed a distortion in the grain boundary arc which was suspected to arise from the space charge layers itself (also observable in Fig. 1.1). This is discussed briefly in MANUSCRIPT I, where an impedance spectrum is simulated using values from a calculated space charge layer defect profile. In the following this simulation of the grain boundary arc is further discussed in view of the space charge effects, firstly showing how the simulation was done.

The specific grain boundary properties derived using BLM and the grain interior conductivity were used to derive Schottky barrier heights for BZY10 (through Eq. (2)). This value together with the dopant concentration, the dielectric constant, the charge of the depleted species and temperature was used to calculate the corresponding defect concentration profiles in the space charge layer. In addition to the BLM the Mott-Schottky approximation (assuming constant acceptor concentration up to the grain boundary core) and an equal mobility in the grain interior and grain boundary were applied as assumptions to simplify the overall picture. The final equation used to calculate the defect profile (also given in MANUSCRIPT I) was

$$\frac{c_{H^+}(x)}{c_{H^+}(\infty)} = \exp\left[-\frac{1}{4}\left(\frac{x-\lambda^*}{L_D}\right)^2\right] \tag{3}$$

where the normalized defect profile in position x in the space charge layer is calculated based on the grain boundary width λ^* and the Debye length, L_D (see MANUSCRIPT I for further derivation). Fig. 2.6 displays a defect profile of BZY10-HP at 250 °C under wet O_2 conditions calculated using Eq. (3). Also included in Fig. 2.6 is the defect profile in the space charge layer divided up in 20 parts. An apparent resistance was calculated from each of these parts using the following equation:

$$R_{gb}^{app}(x) = \frac{2}{\sigma_{gi}\frac{c_{H^+}(x)}{c_{H^+}(\infty)}} \cdot \frac{c_{gi}}{c_{gb}} \tag{4}$$

This equation uses the BLM to calculate apparent resistances from specific resistances. The fractional resistances calculated for each part were then used as individual sub-circuit elements($R_{gb,1}^{app} \dots R_{gb,2}^{app} \dots R_{gb,n}^{app}$). Due to limitations in the ZView software [35] used for the purpose, the number of sub-circuit elements were limited to 14. The 20 parts in Fig. 2.6 were therefore summed into 13 apparent resistances (the 14th sub-circuit element was used for the grain interior). The equivalent circuit used for the simulation is given in Fig. 2.7.
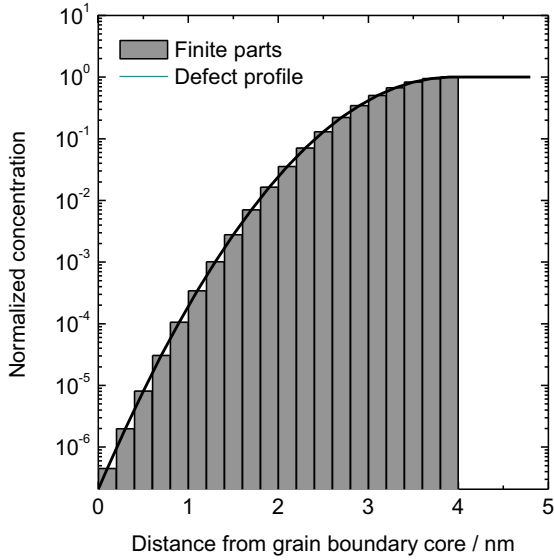
Fig. 2.6. Normalized concentration profile calculated on basis of data for the BZY10-HP sample at 250 °C in wet oxygen. Calculated finite parts of the profile, to derive the grain boundary resistance, are included.
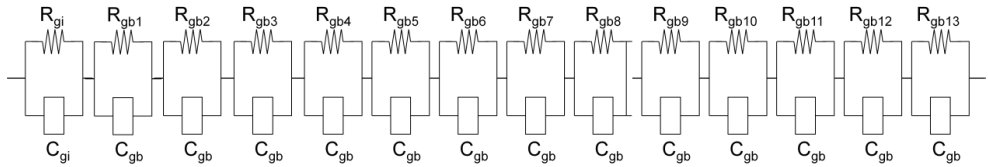
Fig. 2.7. Equivalent circuit used for simulation of the total impedance spectrum.

The grain interior contribution is added in the beginning of the equivalent circuit, and the grain boundary capacitance is held constant for all resistances. The values of these elements were taken from the deconvolution of the original BZY10-HP spectrum at 250 °C in wet O_2.

In addition to 20 finite parts, 40, 80 and 160 finite parts were calculated (all summed to 13 apparent resistances). The impedance spectrum from each simulation is given in Fig. 2.8. As we can see the 80 and 160 finite parts converge towards the same value, which indicates that 80 and 160 finite parts are satisfactory.
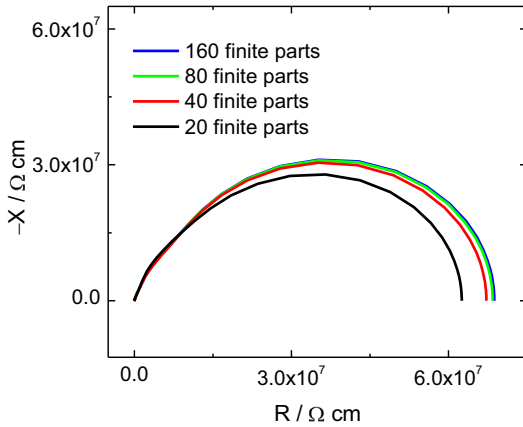
Fig. 2.8. Simulated impedance spectra using the space charge layer concentration profile.

As discussed in MANUSCRIPT I the converged value is somewhat lower than the experimental value, but by changing the effective dopant concentration to 7.5 mol% the simulated spectrum fits the experimental. Furthermore, similar effects of a change in the Schottky barrier height and the dielectric constant on the calculations show that relatively small changes can increase the magnitude of the arc up to the experimental level.

The relatively good agreement indicates that the assumptions made to calculate the concentration profile in the space charge layers are appropriate. If e.g. the mobility in the grain boundary differed from that in grain interior, this would affect the simulation. This is interesting since it indicates that in fact the mobility in the grain interior is similar to that in the grain boundary. Future experimental work, where the abovementioned variables are under complete control, could yield new information on the grain boundary properties such as local mobilities.

3. HYDRATION THERMODYNAMICS OF PROTON CONDUCTORS

A chemical reaction involving the addition of water to a compound can be denoted a hydration reaction. In an oxide which contains oxygen vacancies the hydration is described with the defect chemical reaction given in Eq. (1), given again here for reference.

$$H_2O(g) + v_O^{\bullet\bullet} + O_O^x = 2OH_O^{\bullet} \tag{1}$$

It is the enthalpy of this reaction, the standard molar hydration enthalpy, $\Delta_{hydr}H^0$, which is discussed and measured experimentally in MANUSCRIPT III utilizing a new direct technique; *in-situ* combined calorimetric and gravimetric analysis.

The molar hydration enthalpy of oxygen vacancies varies considerably between materials, but is in general exothermic (negative), which leads to protons dominating at low temperatures and oxygen vacancies at high temperatures. In the search for new materials with high protonic conductivity, the standard molar hydration enthalpy is considered to be important. Relations to material specific properties have therefore been investigated. Kreuer et al. [17] suggested that the oxide's basicity, which describes the affinity for protons, is an important parameter. For perovskites (ABO_3) it has been suggested by Norby et al. [1] that the enthalpy correlates with the difference in electronegativity between the A and B cation (which later was refined to the absolute difference in electronegativity [2]). Recently, a similar correlation with the Goldschmidt tolerance factor was put forward by Bjørheim et al. [2]. All these correlations suffer from considerable scatter. In Fig. 3.1, the correlation put forward by Norby et al. [1] and refined by Bjørheim et al. [2] demonstrates the large scatter, weakening the correlation's predictive power.
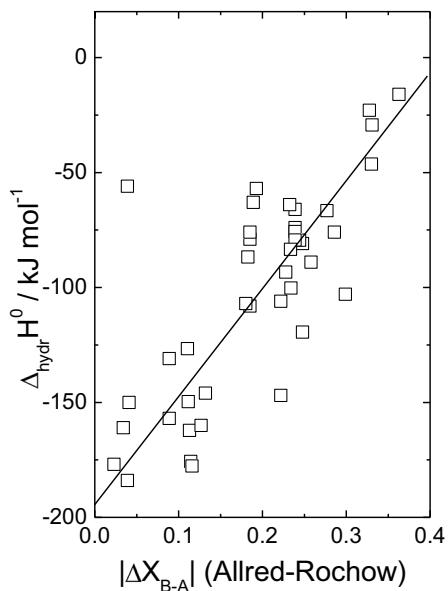
Fig. 3.1. Experimental values of standard molar enthalpy of hydration of oxygen vacancies for a number of perovskite-related oxides, plotted vs. the absolute difference in electronegativity for the occupants of the B and A site. Reported by [1, 2].

The scatter is suggested to depend on the quality of the experimental data. It is therefore an obvious need for a new and more reliable approach to obtain the standard molar hydration enthalpy. Determination of the hydration thermodynamics using an independent calorimetric approach would yield the enthalpy directly. This has been tested [18], but determination of the exact water uptake *ex-situ* to get the molar enthalpy was considered too unreliable (the basic materials involved have poor stability and slow kinetics). Simultaneous thermogravimetry and calorimetry was therefore chosen as the way forward, and in this study an instrument with combined thermogravimetry and differential scanning calorimetry (TG-DSC) has been tested for this purpose. This gives simultaneously both enthalpies and values for the amount of water exchanged, and has therefore a promise to yield data of sufficient accuracy.

This part of the thesis will go into detail on how the indirect techniques used to derive the standard molar enthalpy are applied, with focus on their assumptions. Then, the TG-DSC instrument will be described and the calibration of it explained.

3.1 Measuring $\Delta_{hydr}H^0$ indirectly by thermogravimetry or conductivity

Deriving the standard molar hydration thermodynamics through modelling experimental data with thermodynamic functions requires knowledge of the concentration or the change in concentration of protons. This can be accomplished directly using

thermogravimetry or indirectly by conductivity measurements [36, 37]. Other techniques such as spectroscopy are also possible, but will not be dealt with here. Standard molar hydration thermodynamics are derived, as shown in the following, by modelling the concentrations in terms of a simple defect structure with respect to the hydration reaction given in Eq. (1). This reaction reflects an oxide which takes up protons from ambient water vapour to charge compensate acceptor dopants. The protons thus replace the native charge-compensating defect dominating under dry conditions (e.g. oxygen vacancies). The electroneutrality condition of an acceptor-doped oxide with oxygen vacancies is given as

$$2[v_O^{\bullet\bullet}] + [OH_O^{\bullet}] = [Acc_{Zr}^{/}] = \text{const.} \tag{5}$$

where the square brackets denote molar fractions or volume concentrations, and $Acc_{Zr}^{/}$ denotes an arbitrary acceptor on zirconium site. The acceptor concentration is assumed to be constant throughout the measurements. The equilibrium expression for the reaction between vacancies and water vapour to dissolve protons in Eq. (1) is given by

$$K_{\text{hydr}} = \exp\frac{\Delta_{\text{hydr}}S^{\circ}}{R} \exp\frac{-\Delta_{\text{hydr}}H^{\circ}}{RT} = \frac{x_{OH_O^{\bullet}}^2}{x_{v_O^{\bullet\bullet}}x_{O_O^X}p_{H_2O}} = \frac{[OH_O^{\bullet}]^2}{[v_O^{\bullet\bullet}][O_O^X]p_{H_2O}} \tag{6}$$

As standard reference states, a site fraction of unity and a pressure of 1 bar are defined. Thus, the activities of species in the crystal lattice need to be expressed using site fractions (x), but it so happens that the site concentrations cancel out, so that molar fractions or volume concentrations can be substituted. It is further assumed that

$$[O_O^X] = [O] = \text{const.} \gg 2[v_O^{\bullet\bullet}] + [OH_O^{\bullet}] \tag{7}$$

which gives the following expression for the proton concentration

$$[OH_O^{\bullet}] = \frac{[O]K_{\text{hydr}}p_{H_2O}\left(-1+\sqrt{(K_{\text{hydr}}p_{H_2O})^2 + 8\frac{[Acc_{Zr}^{/}]}{[O]}K_{\text{hydr}}p_{H_2O}}\right)}{4-K_{\text{hydr}}p_{H_2O}} \tag{8}$$

This equation gives an acceptably accurate solution if the dopant and defect levels are moderate or low. The proton concentration comes out in molar fractions or volume concentrations corresponding to the unit that is used for $[O]$ and $[Acc_{Zr}^{/}]$. After calculating the proton concentration it is further possible to derive the oxygen vacancy concentration through the electroneutrality equation and other minority defects by linking appropriate defect-chemical equations to the vacancy concentration. Measuring the concentration of protons can now through Eq. (8) yield the equilibrium constant, and if done against temperature, $\Delta_{\text{hydr}}S^0$ and $\Delta_{\text{hydr}}H^0$. As pointed out by e.g. Krug et al. [38] on their work on Yb-doped $SrCeO_3$ it is

the effective dopant concentration which should be used as the acceptor concentration in Eq. (8). This was identified because a considerably lower uptake of water compared to the nominal dopant concentration was observed. Usually this is interpreted as being due to immobilized protons, to unavailable oxygen vacancies (relaxed/ordered/associated). According to Larring and Norby [39] this observation can also in many cases actually reflect that the conditions of complete saturation have not been met: Full saturation may require a very high water partial pressure or temperatures too low for practical equilibration.

3.1.1 Thermogravimetry

Kreuer et al. [40] studied the standard molar hydration thermodynamics of several acceptor-doped $BaZrO_3$ powders by recording hydration isobars using thermogravimetric analysis (TGA). The data were recorded with a water partial pressure of 0.023 atm in cooling runs where the cooling rates were adjusted to the grain size of the powders and the diffusion coefficient of oxygen vacancies. Due to indications of surface controlled hydration at low temperature the data collection was limited to high temperatures. Fig. 3.2 shows a typical isobaric thermogravimetric measurement of acceptor-doped $BaZrO_3$. Also included in Fig. 3.2 is a plot of equilibrium constants of the hydration reaction calculated from Eq. (8) vs. inverse temperature. The latter plot was used to derive standard molar hydration enthalpies. A direct fitting of the isobars is also possible, however this was not conducted since deviations from ideal behaviour or thermodynamic equilibrium may show up as a deviation from straight line behaviour in the Arrhenius representation. The effective saturation limit taken as the maximum defect concentration observed at low temperature was approximately 100 % in correspondence with the dopant concentration (for all samples). In an earlier study by Kreuer et al. [17] this saturation limit was reported to be ~80% of the dopant concentration for BZY10.
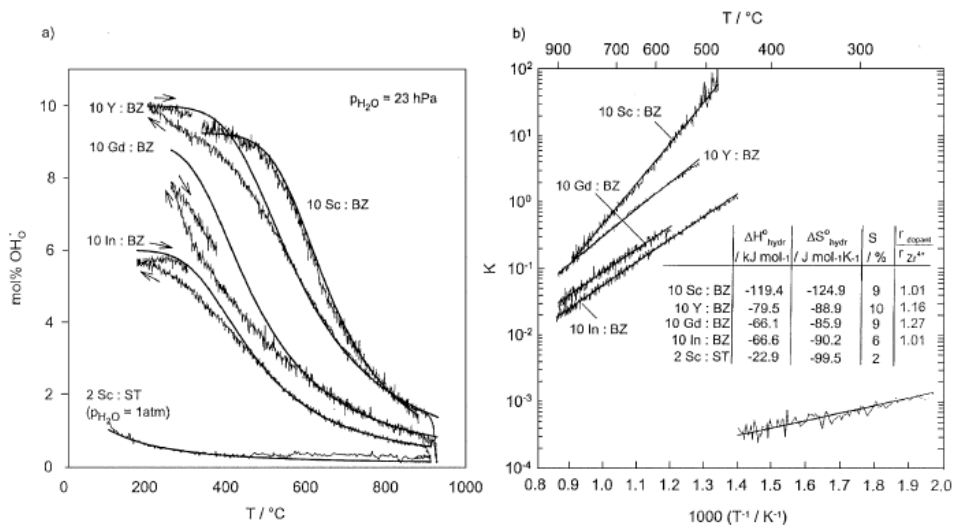
Fig. 3.2. Typical isobaric hydration measured by Kreuer et al. [40] of $BaZrO_3$ with different acceptor dopants. A Sc-doped $SrTiO_3$ (2Sc:ST) sample is also included: a) hydration isobars calculated using Eq. (8), b) equilibrium constant of the hydration reaction calculated using Eq. (6). The molar thermodynamic parameters have been obtained by assuming constant entropy and enthalpy values.

An alternative thermogravimetric method is where the partial pressure of water is varied at a given temperature to yield the equilibrium constant. Results from a typical isothermal measurement performed by Krug et al. [41] on $Ba_3(Ca_{1.18}Nb_{1.82})O_{9-\delta}$ is shown in Fig. 3.3 where distinct steps in relative mass change are obtained when changing the water vapour pressure. From these steps the equilibrium constant is calculated as a function of temperature and the water partial pressure, which furthermore yields the standard molar hydration enthalpy through a van 't Hoff plot. Schober et al. [42] used this method on BZY10, and determined the solubility limit of water to 83.3 % of the dopant concentration.

Fig. 3.3. Typical isothermal thermogravimentric measurement by Krug et al. [41] on the complex perovskite $Ba_3(Ca_{1.18}Nb_{1.82})O_{9-\delta}$.

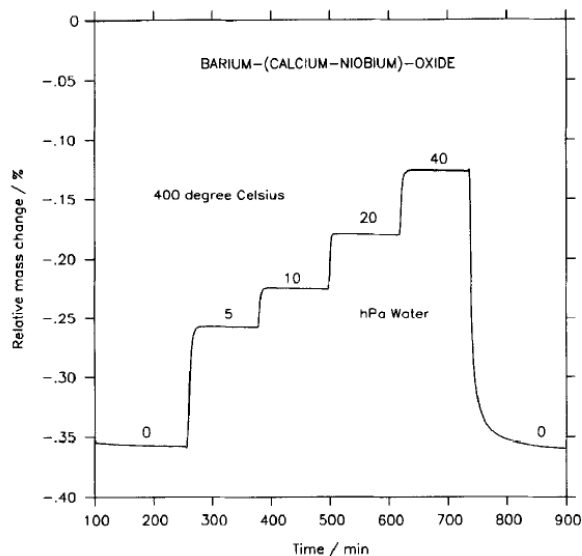Some disagreement exists as to which method that yields the best results, although the isobaric approach seems to have been adopted in recent gravimetric studies [43]. From the thermogravimetric approaches exemplified above it is in principle two main challenges that give rise to uncertainties; to ensure equilibrium measurements and to decide the maximum solubility (effective acceptor concentration).

3.1.2 Conductivity

In a study of protons in $LaErO_3$ Larring and Norby [37] described the main principles of using conductivity measurements to derive standard molar hydration thermodynamics. They also listed some assumptions employed, namely i) full solubility of the dopants, ii) the defects are treated as being in an ideal dilute solution and iii) the conductivities are assumed to represent only grain interior conduction throughout the temperature range. In addition, partial conductivities need to be known (when the total conductivity is not purely protonic), and possible influences from grain boundary and electrode resistances must be excluded. Compared to the thermogravimetric methods mentioned above this method is more complex and may yield data with larger uncertainties. However, as mentioned in MANUSCRIPT III, this indirect method is particularly useful in cases where the water uptake is below the useful sensitivity, accuracy, or stability of thermogravimetric analysis. The conductivity generally gives enthalpies related to concentration as well as to mobility, and thus needs a transition in defect structure that allows deconvolution in the two. Ideally, the mobility of defect is independent of the concentration, and the conductivity measurements can therefore in addition to thermodynamics give useful information on proton mobilities.

When the standard molar hydration enthalpy is modelled from the partial proton conductivity isobars (also taking isothermal measurements vs. p_{O_2} and p_{H_2O} into account) the model expressions used is derived from Eq. (6), Eq. (8) and the following equation:

$$\sigma_{OH_O^\bullet} = Fc_{OH_O^\bullet}u_{OH_O^\bullet} = F[OH_O^\bullet]\delta_M u_{0,OH_O^\bullet}\frac{1}{T}\exp\left(\frac{-\Delta_m H_{OH_O^\bullet}}{RT}\right) \qquad (9)$$

Here $\sigma_{OH_O^\bullet}$, F, $c_{OH_O^\bullet}$, $u_{OH_O^\bullet}$, are the proton conductivity, Faraday constant, concentration and charge mobility, respectively, and where $[OH_O^\bullet]$ is the molar proton concentration, δ_M the density of the material, $u_{0,OH_O^\bullet}$ is the pre-exponential of charge mobility and $\Delta_m H_{OH_O^\bullet}$ is the enthalpy of migration. If the material is a pure proton conductor, the total conductivity may be used for this purpose. If the material is a mixed conductor, the partial proton conductivity may be obtained by transport number measurements (e.g. the EMF method [44]). Alternatively, the total conductivity may be modelled as a sum of partial conductivities, each with an expression like Eq. (9) containing the mobility terms and an appropriate solution for the concentration of the defect.

A study by Haugsrud and Norby [45] on proton conduction in rare-earth ortho-niobates and ortho-tantalales shows the feasibility of the conductivity method to derive hydration thermodynamics. The materials under investigation have dopant solubility limits < 1 mol%. Detection of the water uptake with thermogravimetry is therefore difficult. By fitting measured isobars of partial conductivities (obtained by e.g. EMF method [44]) or total conductivity to the model expressions, the molar entropy and enthalpy of hydration were obtained with reasonable significance (± 10 kJ mol^{-1}).

3.1.3 Evaluation of the indirect techniques

The above techniques are examples of methods which measure neither the entropy nor enthalpy nor the defect chemical reaction. Instead they measure the equilibrium constant K, in this case K_{hydr}. Alternatively, this can be expressed as the standard Gibbs energy change, $\Delta_{hydr}G^0$. By assuming ideality and that the entropy and enthalpy are constant with temperature, these can be obtained from van 't Hoff plots of $\ln K_{hydr}$ vs $1/T$ or of $\Delta_{hydr}G^0$ plotted vs. T. The measured data can be modeled directly with such ideal expressions for K_{hydr} and $\Delta_{hydr}G^0$ built in, but this makes principally no difference; the assumptions are the same. The question of obtaining entropies and enthalpies from these methods rests with the appropriateness of the assumption. Deviations from ideality need therefore to be considered, and such deviations may be expressed by excess functions. When water is dissolved according to Eq. (1) one excess term comes from the interaction between $OH_O^\bullet$, $v_O^{\bullet\bullet}$ and O_O^x. Another excess mixing term involved in the hydration comes from the formation of defect associates such as $(v_O Y_{Zr})^\bullet$. Such excess mixing terms can be handled by applying solution models. The regular solution model is the simplest, where the excess entropy of mixing is assumed to be ideal, while the excess enthalpy is not. Then the molar Gibbs energy is

expressed by an additional interaction term including the coefficient Ω, which yields the extra energy of interaction between the species that constitute the solution. These excess mixing terms can under certain conditions become important for the hydration thermodynamics. One example is formation of the $(v_O Y_{Zr})^\bullet$ complex, which becomes important at high dopant concentrations. The excess function is positive and the trapped oxygen vacancies will affect the hydration enthalpy effectively towards less negative values [1]. In practice, hydration then takes place with the enthalpy of hydration plus the enthalpy of dissociation of the dopant-oxygen vacancy associate. Such an excess term can describe the results obtained by Yamazaki et al. [43] as discussed in MANUSCRIPT III.

   If we assume that the water dissolves ideally (which is an adequate approximation at high temperatures and low dopant concentrations), the indirect methods can in principle yield accurate standard molar hydration enthalpies. However scattering in the correlations will be inevitable if inaccuracies in other assumptions are made. To exemplify, the saturation limit of protons ranges from 80 % to complete saturation for BZY10 (as seen in section 3.1.1). This deviation will give significant differences in the obtained molar enthalpy. The indirect methods used to obtain the hydration enthalpy can be summarized to yield accurate values when the following assumptions hold: i) results are obtained under thermodynamic equilibrium, ii) the species involved behave ideally, iii) the water solubility limit (effective dopant concentration) is known and iv) the data obtained are accurate and obtained over sufficient temperature ranges to allow accurate deconvolution of entropy and enthalpy values.

3.2 Measuring $\Delta_{hydr}H^0$ directly by a combined TG-DSC technique

   Most of the assumptions given above for the indirect methods are not relevant for the direct method utilizing an *in-situ* TG-DSC combined measurement. The method is based on measuring the weight change and the heat exchange simultaneously when the reaction occurs. The experimental approach and results are described and discussed in MANUSCRIPT III and will therefore not be discussed further here. However, the instrument setup will be described in more detail and its calibration will be presented.

   The TG-DSC used was a Netzsch STA (Simultaneous Thermal Analyzer) 449 C Jupiter. The instrument was especially designed to operate under high water vapour pressures, and in order to achieve such a high pressure it was equipped with a water vapour generator, (see Fig. 3.4) and a special furnace constructed for high water vapour pressures (see Fig. 3.5).

   The vapour generator, shown in Fig. 3.4, produces internally 100 % vapour in a special evaporation device. The flow of water for evaporation is measured by a mass flow controller for liquids. The liquid water is completely evaporated (at 180 °C) and the vapour is introduced into the furnace by a heated transfer line and heating jacket, which excludes condensation. Because of the gas lines inside the furnace, the vapour or vapour-gas mixture is furthermore preheated to the sample temperature inside the outer flow chamber and guided from the top over the sample; only this vapour or vapour-gas mixture arrives at the sample. This is indicated in Fig. 3.5. If a second gas is used to dilute the water vapour, this can be introduced in two ways, namely within the water vapour generator as shown in Fig. 3.4 controlled by a needle valve, or with in the instrument using the purge gas channel, controlled

by a mass flow controller. Investigation of both routes showed that the latter gave the best stability (lowest "noise").
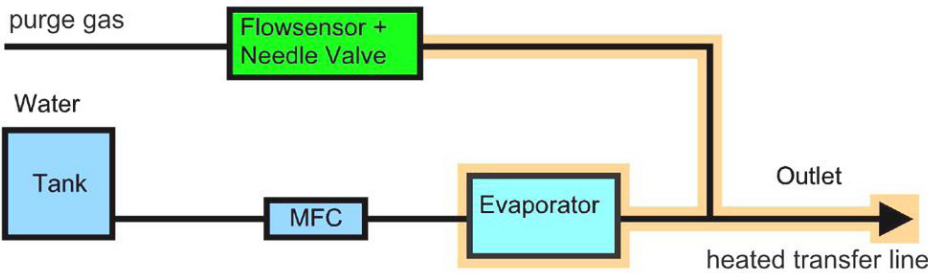

Fig. 3.4. Vapour and gas flow paths in the water vapour generator. Sketch taken from [46].
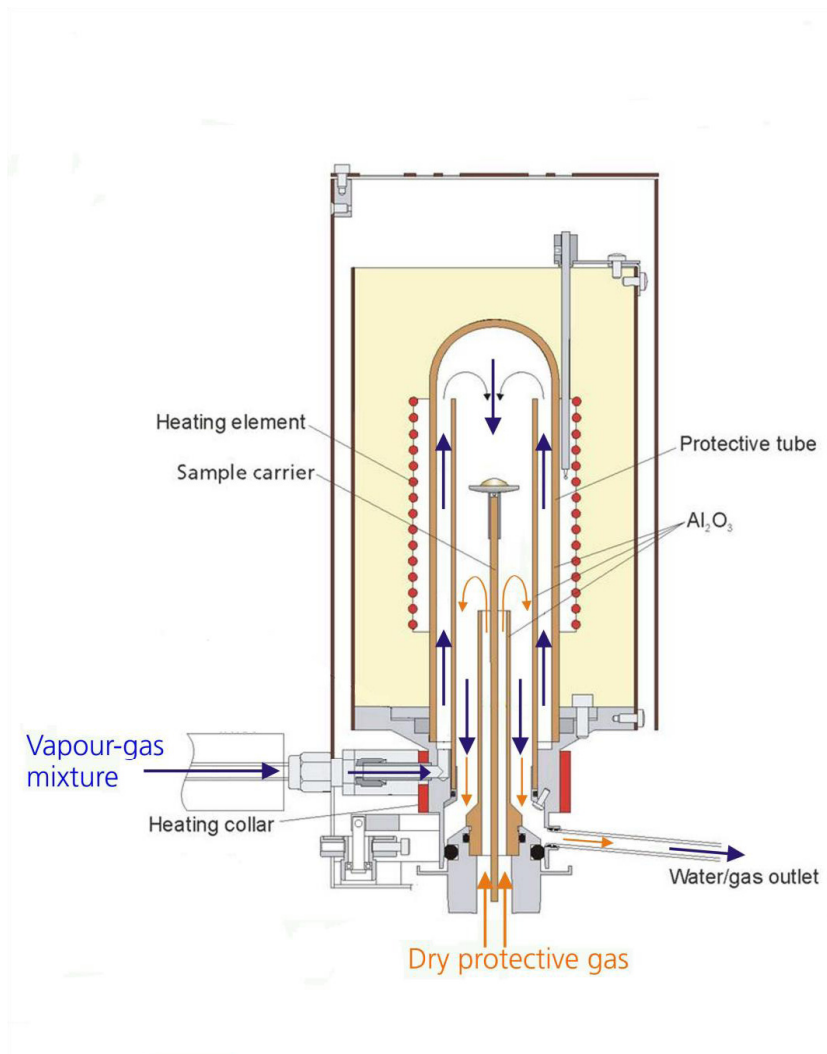
Fig. 3.5. TG-DSC with water vapour furnace. The purge gas used in the experiments is not shown in the sketch, but it is introduced before the heating collar close to the water vapour inlet. Sketch taken from [46].

3.2.1 Calibration of the TG-DSC instrument

Two types of calibration were performed before the TG-DSC instrument was used to measure standard molar hydration enthalpies. The first type for the TG part of the instrument was performed using a built-in automatic calibration procedure. The procedure is simply that a well defined internal mass is put on the balance and the balance signal is compared to the nominal value stored internally in the instrument memory. In the second type for the DSC part, both temperature and DSC sensitivity calibration was performed utilizing known phase transitions of a total of 5 different materials with their transitions spread over a temperature

range suitable for the hydration measurements. The latter will be explained in more detail in the following.

The temperature and DSC sensitivity were calibrated using a selection of substances included in a calibration kit delivered by Netzsch [47]. The substances are given in Table 2 together with their temperature and gravimetric enthalpy of transition.

Table 2. Materials and their temperature and gravimetric enthalpy of transition used in calibration of the TG-DSC instrument delivered by Netzsch [47]. The data are taken from the Netzsch Jupiter 449 C manual [48] which provides further references as given in the table.

Material	Type of transition	Temperature / °C	Enthalpy / J g^{-1}	Reference
RbNO$_3$	Trigonal to cubic	69.2	120.4	[49]
KClO$_4$	Orthorhombic to cubic	300.8	104.9	[49]
Ag$_2$SO$_4$	Hexagonal to orthorhombic	426.4	51.7	[50]
CsCl	Bcc cubic to fcc cubic	476.0	17.22	[50]
BaCO$_3$	Orthorhombic to trigonal	810	94.9	[51]

Standard conditions for the calibration measurements were ambient air with a heating rate of 10 K min^{-1} using Pt/Rh crucibles with the reference crucible empty. An example of a calibration measurement (CsCl) is given in Fig. 3.6 and shows how each sample was heated and cooled three times. Calibration values were calculated from the two latter heating curves which yielded both values for temperature and DSC sensitivity shown as calibration points in Fig. 3.7 and Fig. 3.8, respectively. A polynomial was further applied to the points which resulted in the fitted calibration curve. The polynomial for the temperature is

$$A = 10^{-3}B^0 + 10^{-5}B^1 T_{\text{Exp}} + 10^{-8}B^2 T_{\text{Exp}}{}^2 \tag{10}$$

and for the DSC sensitivity

$$C = \left(D_2 + D_3 \frac{T-D_0}{D_1} + D_4 \left(\frac{T-D_0}{D_1}\right)^2 + D_5 \left(\frac{T-D_0}{D_1}\right)^3 \exp\left(-\frac{T-D_0}{D_1}\right)^2. \tag{11}$$
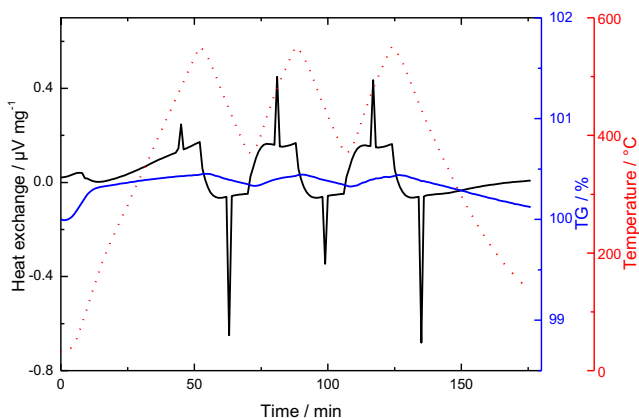
Fig. 3.6. Calibration measurement of CsCl. An average of the area of the endothermic peaks from the second and third heating was used as values in the calibration
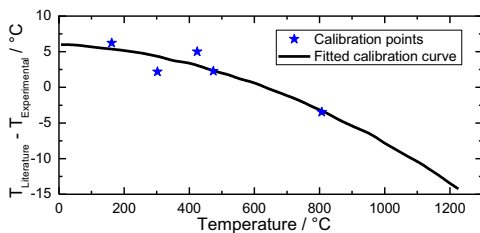
Fig. 3.7. Temperature calibration curve based on measurements of the materials given in Table 2
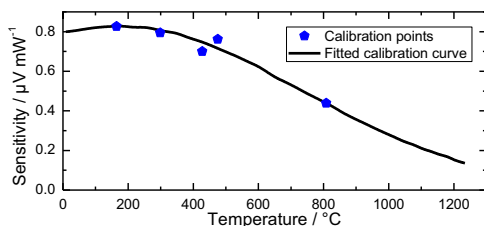
Fig. 3.8. DSC sensitivity calibration curve based on measurements of the materials given in Table 2

The calibration files were loaded into the measurement software before each measurement was started to yield molar enthalpies. Technical data for the instrument with accuracies and reproducibility factors included are given in Table 3, and as can be seen, the enthalpy accuracy is listed as ± 3 %.

Table 3. Resolution of the STA 449 C Jupiter instrument

Measuring unit	
Baseline reproducibility	~ 1μV (± 2.5 mW)
Signal to noise ratio	~ 15 μW
Baseline linearity	3 μV
Temperature accuracy	< 1K
Enthalpy accuracy	± 3 %

4. MANUSCRIPTS

4.1 Manuscript I

Space charge theory applied to the grain boundary impedance of proton conducting $BaZr_{0.9}Y_{0.1}O_{3-\delta}$

Submitted to Solid State Ionics

4.2 Manuscript II

Microstructural characterization and electrical properties of spray pyrolyzed conventionally sintered or hot-pressed $BaZrO_3$ and $BaZr_{0.9}Y_{0.1}O_{2.95}$

Submitted to Solid State Ionics

4.3 Manuscript III

Isothermal measurement of hydration enthalpy of selected proton conductors by simultaneous thermogravimetry and differential scanning calorimetry

Submitted to Physical Chemistry and Chemical Physics (PCCP)

4.4 Manuscript IV

Mobility and concentration of electrons in ZnO studied by measurements of electrical conductivity and thermoelectric power in H2 + H2O atm at high temperatures

In preparation

5. DISCUSSION

This chapter forms extensions of the discussions within the MANUSCRIPT I, II and III on grain boundaries and hydration. Despite the splitting of the thesis into three parts, there are also links and common features. Questions addressed under one part can thus be relevant to the others. For instance, can the value of a grain boundary core hydration enthalpy be obtained using the TG-DSC technique by applying samples of different grain sizes? Is the shallow donor characteristics of hydrogen in ZnO also applicable if space charge effects exist in the ZnO grain boundaries?
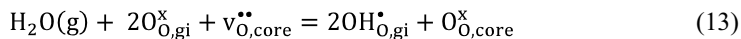
5.1 Grain boundary core hydration

Studies on both perovskites and fluorite type materials have given indications that accumulation of oxygen vacancies is the origin of the positive charge in the grain boundary core [52, 53]. An important question related to the possible difference between the oxide ion and proton conductors is whether the oxygen vacancies in the grain boundary core can be affected by water and be hydrated, and if they can, whether this is different than it is in the grain interior. In MANUSCRIPT I we briefly discussed the hydration of the grain boundary core to explain an observed difference in Schottky barrier height under dry and wet conditions. We suggested one hydration equation which we found to be the most reasonable for grain boundaries in BZY10 (this is mentioned below). In the following we will put forward and discuss some alternative grain boundary core hydration reactions.

Grain boundary core oxygen sites and oxygen vacancies can be hydrated according to the following equation (equivalent to the standard hydration reaction given in Eq. (1)):

$$H_2O(g) + O_{O,core}^x + v_{O,core}^{\bullet\bullet} = 2OH_{O,core}^{\bullet} \tag{12}$$
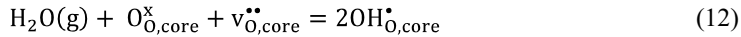
This will annihilate the vacancy and place instead two protons in the core, which in total will keep the charge in the grain boundary unchanged. The grain boundary electrical properties will correspondingly not be changed, and the hydration of the core will therefore be difficult to detect experimentally. This reaction will presumably be operative in parallel with the standard reaction for grain interior when the stability of the oxygen vacancies is equal in the grain boundary core and grain interior. However as discussed (e.g. in MANUSCRIPT I) the oxygen vacancies are expectedly more stable in the grain boundary core. The next proposed reaction is therefore probably less favourable:

$$H_2O(g) + 2O_{O,gi}^x + v_{O,core}^{\bullet\bullet} = 2OH_{O,gi}^{\bullet} + O_{O,core}^x \tag{13}$$

The somewhat opposite reaction to the latter is as follows

$$H_2O(g) + v_{O,gi}^{\bullet\bullet} + 2O_{O,core}^x = O_{O,gi}^x + 2OH_{O,core}^{\bullet} \tag{14}$$
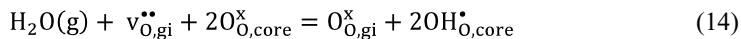
Because the oxygen vacancies decrease the lattice mismatch of the grain boundary core, they are stabilised, and therefore less easily hydrated. Then the grain interior vacancies are instead selectively filled during hydration while the protons may still bond to oxide ions in the grain boundary core, to further reduce the problems of unsatisfied bonds and mismatches. The Schottky barrier height thereby increases under wet conditions. This was thus suggested to be the case for BZY10 as discussed in MANUSCRIPT I.

Finally, we propose a hydration reaction that includes cation vacancies (which might exist due to the large structural disorder) in the core. A cation vacancy may be associated by from one to four protons, the reaction being exothermic and the number thus increasing with decreasing temperature and – obviously increasing p_{H_2O}. The decrease in effective charge is – as before – accounted for by annihilation of oxygen vacancies. At full protonation of the cation vacancy the reaction becomes

$$2H_2O(g) + v_{Zr,core}^{////} + 2v_{O,gi}^{\bullet\bullet} + 2O_{O,core}^{x} = (v_{Zr}4OH_O)_{core}^{x} \qquad (15)$$
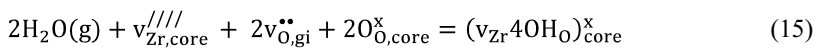
The unprotonated cation vacancies are unfavourable due to their large effective charge, and this will thus drive the protonation. If as before the oxygen vacancies are assumed to be annihilated primarily in the grain interior, the protonation of cation vacancies in the grain boundary core will increase the effective charge in the core, and therefore give an increasing Schottky barrier height.

A grain boundary core hydration will only give a change in the grain boundary conductivity if sites in the grain boundary core are energetically different from grain interior sites so that there is a change in the grain boundary core charge. This is true for the reaction in Eq. (13), (14), and (15). Only in Eq. (13) does the Schottky barrier height decrease when hydrated, which leads to a correspondingly lower grain boundary resistance, favourable application-wise. In general it seems however that the Schottky barrier height expectedly increases during hydration. This may in fact be the reason for the generally higher grain boundary resistance in proton conductors compared to oxide ion conductors.

5.2 Grain boundary hydration thermodynamics

In the former section different grain boundary hydration reactions were suggested and the reaction in Eq. (14) (also given in MANUSCRIPT I) seemed to be the reaction governing the grain boundary hydration of BZY10. However, this conclusion must be taken with caution until other experimental results are available to support it. The hydration thermodynamics would give an indication on which hydration reaction that could be applied. If we look at the different reactions given in Eq. (12) to Eq. (15) we can anticipate that the standard molar enthalpy of the three first reactions should lie in the same region. An experimental technique that possibly can give information on the grain boundary hydration molar enthalpy is the combined calorimetric-thermogravimetric method used in MANUSCRIPT III. One can here imagine that the molar hydration enthalpy is measured directly on dense samples (to avoid effects of pore surfaces) with different grain size. The difference in the molar hydration

enthalpy of a nano-grained sample and a sample with large grains would reflect the grain boundary standard molar hydration enthalpy. The molar grain boundary hydration value can possibly be extracted by plotting the enthalpy as a function of grain size, and extrapolating to "zero" grain size, reflecting only grain boundaries. One can also imagine that the molar grain boundary hydration enthalpy can be obtained indirectly using impedance spectroscopy through which the specific grain boundary conductivities can be calculated. These conductivities can then be fitted to defect chemical models as explained in section 3.1. To apply such a method would require several assumptions which have large uncertainties such as the level of maximum solubility (the effective concentration of oxygen vacancies in the grain boundary). However, to see the relative magnitude of the molar grain boundary hydration enthalpy we have done an attempt to fit the grain boundary conductivity vs. water partial pressure dependencies and the grain boundary conductivities vs. temperature to the defect chemical model discussed in section 3.1. The preliminary result shows values $(\Delta_{hydr}H^0 \sim$ - 40 – -100 kJ mol^{-1}) in the same range as that obtained through the TG and TG-DSC techniques. This gives a first indication that the grain boundary core hydrates relatively similarly to the grain interior.

If the molar hydration enthalpies correlate with the Goldschmidt tolerance factor, as shown by Bjørheim et al. [2] protons are stabilized by structural distortions to a larger extent than oxygen vacancies. If this is applied to the grain boundary hydration thermodynamics, where the structural distortion is obvious, the corresponding grain boundary hydration enthalpy should be larger in the grain boundary than in the grain interior. The structural distortion which stabilizes the protons in non-cubic perovskites can most probably be considered small compared to the structural mismatches in a grain boundary (involving e.g. dangling bonds). The grain boundary hydration enthalpy can from this be expected to be dependent, and probably increase with increasing misfit of the grain boundary.

5.3 Hydrogen energy level in grain boundaries

The proton transport over a resistive grain boundary can in principle involve a red-ox reaction, especially if the band gap in the grain boundary core is smaller than in the grain interior. If in fact this applies, one must also consider different relative energy levels in the band gap of the hydrogen in the grain interior compared to the grain boundary. Hydrogen in such a sample might then behave differently, e.g. going from a shallow donor in the grain interior to a deep donor in the grain boundary. Imagine that this could be the case for the grain boundaries in ZnO; the hydrogen in a nano grained sample dominated by grain boundaries would then behave more amphoteric, which in principle would facilitate p-type conducting ZnO. In a recent study by Wang et al. [54] ZnO films were obtained in which the grain boundaries were found to be p-type conducting under oxidizing conditions. This was attributed to chemisorbed oxide ions, which caused an upward band bending near the grain boundary; negative charge of the oxide ions yielded a negative charged grain boundary core. In Fig. 5.1 the schematic illustration of the space charge effect in the grain boundaries of ZnO as explained by Wang et al. is shown. Due to the existence of a negatively charged grain

boundary core, mobile electrons are depleted and mobile electron holes are accumulated in the space charge layers, which causes p-type conduction in the grain boundaries.
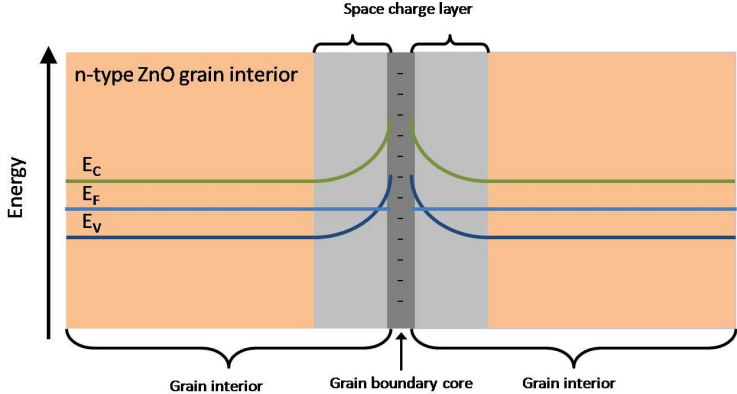

Fig. 5.1. Schematic illustration of the space charge effect in grain boundaries of ZnO as explained by Wang et al. [54]. A band bending causes the grain boundary Fermi level to approach the valence band edge and finally merge into the valence band. This causes a p-type conduction in the grain boundaries.

As suggested by Van de Walle et al. [3] there exists a universal alignment of the hydrogen transition level (between the proton (H$^+$) and the hydride ion (H$^-$), the neutral hydrogen level is always higher in energy), denoted $\varepsilon(+/-)$, for semiconductors indicating whether hydrogen exists as a shallow or deep donor/acceptor. For ZnO this level is calculated to lie within the conduction band, and hydrogen acts consequently always as a shallow donor. However, if this level is relatively close to the conduction band edge, and there is a band bending in the grain boundaries according to the explanation of Wang et al., the transition level can be within the band gap of the grain boundaries. This is schematically illustrated in Fig. 5.2. Hydrogen would then act as a deep donor in the grain boundaries of ZnO, and not contributing directly to the n-type conduction. Other intrinsic defects would then dominate the grain boundary conductivity, and these could yield the p-type conduction. This latter explanation of the observed p-type conduction in the grain boundaries of thin film ZnO is different to that explained by Wang et al. when the role of hydrogen is taken into account.
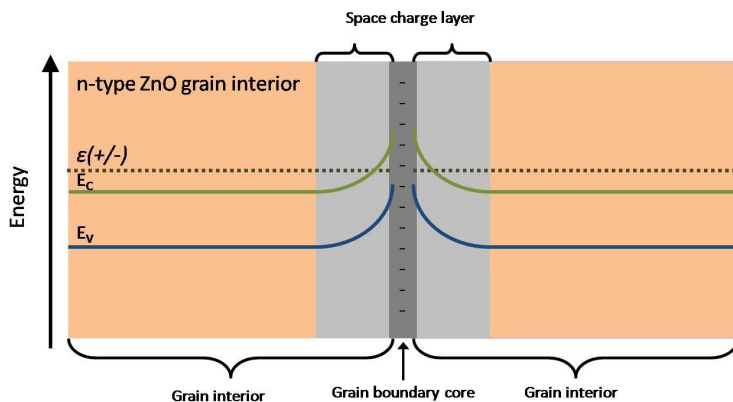
Fig. 5.2. Schematic illustration of the space charge effect in grain boundaries of ZnO with a band bending of the conduction and valence band in the space charge layers due to a negative charged grain boundary core. The $\varepsilon(+/-)$ transition level of hydrogen is included.

5.4 Correlations of the hydration enthalpy

In Fig. 5.3 we see results obtained in MANUSCRIPT III included in the correlation by Norby et al. [1] (modified by Bjørheim et al. [2]) with difference in absolute electronegativities. The correlation by Bjørheim et al. [2] with the tolerance factor is included in MANUSCRIPT III. The measured standard molar enthalpies from this study are in agreement with molar enthalpies obtained in the literature. If we now assume that this indicates that the obtained literature values in Fig. 5.3 are correct, the scatter – or rather the deviation from the linear regression line - in the correlation plots is actual. The linear correlation is empirical, and thus we probably are missing out other underlying and finer relationships. We need therefore to look more closely into the suggested correlations. Kreuer et al. [55] suggests that the variation in hydration enthalpy is dominated by the formation energy of protonic defects, $E_{\mathrm{OH_O^{\bullet}}}^{\mathrm{for}}$, while the variation in formation energy of oxygen vacancies $E_{\mathrm{v_O^{\bullet\bullet}}}^{\mathrm{for}}$, is considered small. In this case, the hydration enthalpy is only governed by decreasing Bronsted basicity of the oxide, i.e. the electronegativity of the cations in interaction with the lattice oxygen. They observed an increasingly exothermic hydration enthalpy in the order titanates – niobates –zirconates – stannates – cerates which supported the role of basicity. (A problem here is that a quantitative measure of the basicity of ternary oxides such as perovskites does not exist).

In the correlation put forward by Norby et al. [1] the hydration gets more exothermic with decreasing difference in the electronegativity between the B and A cation radii. This correlation shows an increasingly exothermic hydration when the charge density on the oxide ions (most basic and high proton affinity) increases, which is the case when the electronegativities are similar. An observed increasing stability with decreasing radius of the A cation, explained by an increase in the OH-bond length due to the smaller cations giving a denser oxygen sub lattice, led to the correlation put forward by Bjørheim et al. [2], which also

is in agreement with the Norby correlation. Here, the Goldschmidt tolerance factor, which is a measure of the deviation from the perfect cubic perovskite was used as a measure of the stability. Combinations which yield a fuller description with less scattered correlation might exist. However, to find such a combination is challenging, and although several attempts have been made, none that gives less scatter has been found. There have also been raised questions on whether the hydration is dominated by the formation energy of the protonic defects as mentioned by Kreuer et al. [55], and also whether the formation energy of oxygen vacancies influences [56]. A similar competition between the oxygen vacancies and protons has been observed in sesquioxides by Larring et al. [16]. Since the hydration is dependent on the ratio between these formation energies, a variation within these energies can influence the correlation. However little data of formation energies of oxygen vacancies in perovskites are known and such a correlation is therefore difficult to investigate. Calculating these energies using density functional theory (DFT) may be a useful approach.
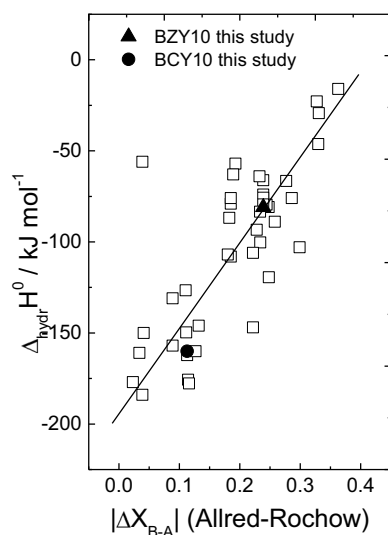

Fig. 5.3. Standard molar hydration enthalpy of ABO_3 perovskites as a function of the absolute value of the difference in electronegativity of the cations from Bjørheim et al. [2]. The experimental values obtained in this study are included.

6. CONCLUSIONS

In the present thesis thermodynamics and transport of protons in oxides have been investigated under various conditions using different techniques. Grain boundary resistance and hydration thermodynamics of proton conductors, as well as hydrogenation and transport of electrons in ZnO have been the main topics.

The grain boundaries in 10 % Y-doped $BaZrO_3$, sintered by spark plasma and hot pressing and conventionally sintered nominally undoped $BaZrO_3$ showed high proton resistivity and an additional n-type electronic conductivity under reducing conditions, and an accumulation of negatively charged Y-dopants for the doped cases. These all together suggests the possible existence of a charged grain boundary core with adjacent space charge layers. Additionally, a distortion in impedance spectra in the grain boundary arc was found to support this suggestion. A space charge model was applied and gave the space charge layer defect profile. Schottky barrier heights were calculated for two doped samples and were 0.51 V and 0.62 V at 300 °C in a humidified oxygen atmosphere. A difference in Schottky barrier height under wet and dry conditions was ascribed to a hydration of grain boundary core oxygen sites on the cost of grain interior oxygen vacancies. The obtained grain interior conductivities were in agreement with earlier reported literature values and reflect mixed proton and electron hole conductivities. For the undoped case, a larger ratio of p-type electronic to protonic conduction in the grain boundaries was observed, contrary to the prediction of simple defect chemistry and space charge layer theory.

A standard molar hydration enthalpy of oxygen vacancies has been studied for the first time with a combined thermogravimetric-calorimetric approach using a novel TG-DSC instrument. The obtained molar hydration enthalpy of 10 % Y-doped $BaZrO_3$ was investigated at 300-900 °C and was found constant at -81±4 kJ mol^{-1} over this range. The molar hydration enthalpy of 10 % Y-doped $BaCeO_3$ at 600 °C was found to be -170±6 kJ mol^{-1}. Both values are in good agreement with the majority of literature data obtained by indirect equilibrium methods.

The electrical properties of polycrystalline and single crystal ZnO in hydrogen containing atmospheres at high temperatures is determined by hydrogen which dissolves and ionizes fully to protons and electrons. Above ~450 °C, the hydrogen defects were in equilibrium with the surroundings, and the concentration of protons and electrons increased with temperature and with $p_{H_2}^{1/4}$ in accordance with the defect thermodynamics from literature. Hydrogen was found to freeze in at temperatures below ~450 °C, which resulted in a high internal hydrogen pressure during further cooling. The local strain from the presence of frozen in neutral H_2 species was suggested to cause an observed modest reduction in the mobility and conductivity of electrons. The levels of defect concentrations and electron mobility based on the thermoelectric power were one order of magnitude off compared with established literature, suggesting that the prevailing view of entropy of electrons in ZnO may be different from that of a free electron gas.

7. LIST OF ABBREVATIONS

a	Activity
BET	Brunauer, Emmett and Teller
BCY10	10 mol% yttrium doped barium cerate $BaCe_{0.9}Y_{0.1}O_{3-\delta}$
BLM	Brick layer model
BZY10	10 mol% yttrium doped barium zirconate $BaZr_{0.9}Y_{0.1}O_{3-\delta}$
C_{gb}	Grain boundary capacitance
C_{gi}	Grain interior capacitance
$c_{H^+}(\infty)$	Proton concentration in grain interior
$c_{H^+}(x)$	Proton concentration at distance x
C_{stray}	Parasitic capacitance
δ	Density
ΔG^0	Standard molar Gibbs energy
ΔH^0	Standard molar hydration enthalpy
ΔS^0	Standard molar hydration entropy
$\Delta\varphi(0)$	Schottky barrier height
$D_{H^+}^*$	Self diffusion coefficient of electrons
DSC	Differential scanning calorimetry
$|\Delta X_{B-A}|$	Absolute difference in electronegativity of element B and A
e	Elementary electrical charge
$E_{A,gb}$	Grain boundary activation energy
$E_{A,gi}$	Grain interior activation energy
EDS	Electron dispersive spectroscopy
η_{H^+}	Electrochemical potential of protons
F	Faraday constant
FEG-SEM	Field emission gun – scanning electron microscopy
h	Planck's constant
HP	Hot pressed
HRTEM	High resolution transmission electron microscopy
IR	Infrared spectroscopy
K	Equilibrium constant
k_B	Boltzmann constant
L_D	Debye length
λ^*	Effective grain boundary width
$\mu_{H^+}^0$	Standard chemical potential of protons
μ_0	Pre-exponential of charge mobility
m^*	Electron effective mass
N_c	Effective density of states
p_{H_2}	Partial pressure of hydrogen
p_{O_2}	Partial pressure of oxygen
p_{H_2O}	Partial pressure of water

$\varphi(\infty)$	Electrostatic potential in grain interior
$\varphi(x)$	Electrostatic potential at distance x
Q	Thermoelectric power
q	Elementary electrical charge
$Q(x)$	Net charge density at distance x
r	Characteristic number for the scattering mechanism
$\rho(x)$	Resistivity at distance x
R_{gb}	Grain boundary resistance
R_{gi}	Grain interior resistance
RMS	Root mean square
SAED	Selected area electron diffraction
SEM	Scanning electron microscopy
σ_{gb}	Grain boundary conductivity
σ_{gi}	Grain interior conductivity
SPS	Spark plasma sintered
STA	Simultaneous thermal analyzer
τ_m	Relaxation time
TEM	Transmission electron microscopy
TG	Thermogravimetry
u_n	Electron mobility
XRD	X-ray diffraction
z	Number and sign of charge carriers

8. LIST OF REFERENCES FOR CHAPTER 1-3 AND 5

1. T. Norby, M. Widerøe, R. Glöckner and Y. Larring, *Dalton Trans.* (2004) (19), p. 3012.
2. T.S. Bjørheim, A. Kuwabara, I. Ahmed, R. Haugsrud, S. Stølen and T. Norby, *Solid State Ionics* (2009) (doi:10.1016/j.ssi.2009.04.013).
3. C.G. Van de Walle and J. Neugebauer, *Nature (London, United Kingdom)* **423** (2003) (6940), p. 626.
4. S.P.S. Badwal, *Solid State Ionics* **76** (1995) (1,2), p. 67.
5. R. Gerhardt and A.S. Nowick, *Journal of the American Ceramic Society* **69** (1986) (9), p. 641.
6. M. Goedickemeier, B. Michel, A. Orliukas, P. Bohac, K. Sasaki, L. Gauckler, H. Heinrich, P. Schwander and G. Kostorz, *Journal of Materials Research* **9** (1994) (5), p. 1228.
7. J. Maier, *Progress in Solid State Chemistry* **23** (1995) (3), p. 171.
8. A. Tschope, *Solid State Ionics* **139** (2001) (3,4), p. 267.
9. R. Waser, *Solid State Ionics* **75** (1995), p. 89.
10. X. Guo and Y. Ding, *Journal of the Electrochemical Society* **151** (2004) (1), p. J1.
11. X. Guo and R. Waser, *Progress in Materials Science* **51** (2006) (2), p. 151.
12. T. Holbling and R. Waser, *Journal of Applied Physics* **91** (2002) (5), p. 3037.
13. S. Kim, J. Fleig and J. Maier, *Physical Chemistry Chemical Physics* **5** (2003) (11), p. 2268.
14. H.J. Park and S. Kim, *Journal of Physical Chemistry C* **111** (2007) (40), p. 14903.
15. M. Vollman and R. Waser, *Journal of the American Ceramic Society* **77** (1994) (1), p. 235.
16. Y. Larring and T. Norby, *Solid State Ionics* **77** (1995), p. 147.
17. K.D. Kreuer, *Solid State Ionics* **125** (1999) (1-4), p. 285.
18. C. Haavik and T. Norby, *unpublished work*.
19. D.G. Thomas and J.J. Lander, *Journal of Chemical Physics* **25** (1956), p. 1136.
20. A.R. Hutson, *Phys. Rev.* **108** (1957) (222).
21. J. Maier, *International Journal of Materials Research* **99** (2008) (1), p. 24.
22. X. Guo, W. Sigle, J. Fleig and J. Maier, *Solid State Ionics* **154-155** (2002), p. 555.
23. X. Guo, W. Sigle and J. Maier, *Journal of the American Ceramic Society* **86** (2003) (1), p. 77.
24. X.L. Guo, H. Tabata and T. Kawai, *Journal of Crystal Growth* **223** (2001) (1-2), p. 135.
25. X. Guo, S. Mi and R. Waser, *Electrochemical and Solid-State Letters* **8** (2005) (1), p. J1.
26. R. Meyer, X. Guo and R. Waser, *Electrochemical and Solid-State Letters* **8** (2005) (10), p. E67.
27. C. Kjølseth, *Unpublished work*, (2009).
28. S. Kim and J. Maier, *Journal of the Electrochemical Society* **149** (2002) (10), p. J73.

29.   S. Rodewald, J. Fleig and J. Maier, *Journal of the American Ceramic Society* **84** (2001) (3), p. 521.

30.   P. Babilo, T. Uda and S.M. Haile, *Journal of Materials Research* **22** (2007) (5), p. 1322.

31.   S.B.C. Duval, P. Holtappels, U.F. Vogt, E. Pomjakushina, K. Conder, U. Stimming and T. Graule, *Solid State Ionics* **178** (2007) (25-26), p. 1437.

32.   F. Iguchi, T. Tsurui, N. Sata, Y. Nagao and H. Yugami, *Solid State Ionics* **180** (2009) (6-8), p. 563.

33.   H.J. Park, C. Kwak, K.H. Lee, S.M. Lee and E.S. Lee, *Journal of the European Ceramic Society* **29** (2009), p. 2429.

34.   S.M. Haile, D.L. West and J. Campbell, *Journal of Materials Research* **13** (1998) (6), p. 1576.

35.   D. Johnson, ZView, *Scribner Associates, Inc.* (2007).

36.   K.D. Kreuer, T. Dippel, Y.M. Baikov and J. Maier, *Solid State Ionics* **86-88** (1996) (Pt. 1), p. 613.

37.   Y. Larring and T. Norby, *Solid State Ionics* **70-71** (1994) (1-4), p. 305.

38.   F. Krug, T. Schober and T. Springer, *Solid State Ionics* **81** (1995) (1,2), p. 111.

39.   T. Norby and Y. Larring, *Current Opinion in Solid State & Materials Science* **2** (1997), p. 593.

40.   K.D. Kreuer, S. Adams, W. Munch, A. Fuchs, U. Klock and J. Maier, *Solid State Ionics* **145** (2001) (1-4), p. 295.

41.   F. Krug and T. Schober, *Solid State Ionics* **92** (1996) (3,4), p. 297.

42.   T. Schober and H.G. Bohn, *Solid State Ionics* **127** (2000) (3,4), p. 351.

43.   Y. Yamazaki, P. Babilo and S.M. Haile, *Chem. Mater.* **20** (2008) (20), p. 6352.

44.   D.P. Sutija, T. Norby and P. Bjoernbom, *Solid State Ionics* **77** (1995), p. 167.

45.   R. Haugsrud and T. Norby, *Nature Materials* **5** (2006) (3), p. 193.

46.   Kaisersberger, Netzsch Water Vapor Furnace and Humidity Generators - Manual, (2008).

47.   Netzsch-GmbH, *Calibration Kit: 6.223.5-91.2.*

48.   Netzsch, *Proteus - Thermal Analysis* **V 4.8.5** (2008).

49.   Netzsch, derived from measurements carried by Netszch with a DSC 200 previously calibrated for temperature with Hg, In, Sn, Bi, Zn and CsCl.

50.   A.P. Gray, *Proceedings, Fourth ICTA* **3** (1974).

51.   W. Eysel and K.-H. Breuer, *Thermochemica Acta* **52** (1982), p. 317.

52.   N.D. Browning, J.P. Buban, H.O. Moltaji, S.J. Pennycook, G. Duscher, K.D. Johnson, R.P. Rodrigues and V.P. Dravid, *Applied Physics Letters* **74** (1999) (18), p. 2638.

53.   Y. Lei, Y. Ito, N.D. Browning and T.J. Mazanec, *Journal of the American Ceramic Society* **85** (2002) (9), p. 2359.

54.   B. Wang, J. Min, Y. Zhao, W. Sang and C. Wang, *Applied Physics Letters* **94** (2009) (19), p. 192101/1.

55.   K.D. Kreuer, *Annual Review of Materials Research* **33** (2003), p. 333.

56.   T.S. Bjørheim, Master thesis, Deparment of Chemistry , University of Oslo (2008).